

**PREPARATION AND STUDY OF THIN RDX FILMS STANDARDS ON
VARIOUS SUBSTRATES DEPOSITED BY SPIN COATING
TECHNOLOGY**

By

José L. Ruiz Caballero

A thesis submitted in partial fulfillment of the requirements for the degree of

DOCTOR OF PHILOSOPHY

in

APPLIED CHEMISTRY

UNIVERSITY OF PUERTO RICO
MAYAGÜEZ CAMPUS

May, 2017

Approved by:

Nairmen Mina Camilde, Ph.D
Member, Graduate Committee

Date

Alberto Santana Vargas, Ph.D
Member, Graduate Committee

Date

Ricardo Infante Castillo, Ph.D
Member, Graduate Committee

Date

Samuel P. Hernández Rivera, Ph.D
President, Graduate Committee

Date

Rafael A. Rodríguez Solís, Ph.D
Representative of Graduate Studies

Date

Enrique Meléndez, Ph.D
Chairperson of the Department

Date

Abstract of Dissertation Presented to the Graduate School
of the University of Puerto Rico in Partial Fulfillment of the
Requirements for the Degree of Doctor of Philosophy

**PREPARATION AND STUDY OF THIN RDX FILMS STANDARDS ON
VARIOUS SUBSTRATES DEPOSITED BY SPIN COATING
TECHNOLOGY**

By

José L. Ruiz Caballero

May 2017

Advisor: Samuel P. Hernández Rivera
Major Department: Chemistry

The highly energetic material (HEM) hexahydro-1,3,5-trinitro-s-triazine, also known as RDX, has two stable conformational polymorphs at room temperature: α -RDX (molecular conformation of $-\text{NO}_2$ groups: axial-axial-equatorial) and β -RDX (molecular conformation of $-\text{NO}_2$ groups: axial-axial-axial). Both polymorphs can be formed by crystallization upon deposition on stainless steel (SS) and gold (Au) substrates using a spin coating methodology. α -RDX is the most stable crystal form at room temperature and ambient pressure. However, β -RDX, which has been reported to be difficult to obtain in bulk form at room temperature, was readily formed.

Reflection-absorption infrared spectroscopy (RAIRS) measurements of RDX-coated substrates provided spectral markers that were used to distinguish between the conformational polymorphs on large surface areas of the substrates. Raman spectroscopy was employed to examine small areas where the intensity is proportional to the height of the structures for RDX. Spectral features were interpreted and classified by using principal component analysis (PCA). The results of these spectral analyses provided good correlation with the values reported in the literature. Optimized conditions to generate nearly only β -RDX

crystalline films using increasing rotational speeds on these substrates were obtained. PCA was also applied to predict percentages of polymorphs present in experimental samples.

On the other hand, the optical properties for crystalline films of the highly energetic material (HEM) previously cited as RDX, deposited on gold (Au) and stainless steel (SS) substrates are also presented. The optical properties obtained in the present study correspond to thin film samples of predominantly β -RDX polymorph. The infrared spectroscopic intensities measured showed significant differences in the β -RDX crystalline films deposited on the two substrates with respect to the calculated real part of refractive index. The β -RDX/Au crystalline films have a high dynamic response, which is characterized by the asymmetric stretching mode of the axial nitro groups, whereas for the β -RDX/SS crystalline films, the dynamic response was mediated by the $-\text{N}-\text{NO}_2$ symmetric stretch mode. This result provides an idea of how the electric field vector propagates through the β -RDX crystalline films deposited on the two substrates. Applications for the results obtained suggest the modification of existing vibrational spectroscopy-based spectral libraries for defense and security applications. Understanding the effects of polymorphism of HEMs will result in the attainment of higher confidence limits in the detection and identification of explosives especially at trace or near trace levels.

Resumen de Disertación Presentado a Escuela Graduada
de la Universidad de Puerto Rico como requisito parcial de los
Requerimientos para el grado de Maestría en Ciencias

TITULO DE LA TESIS

Por

José L. Ruiz Caballero

Mayo 2017

Consejero: Samuel P. Hernández Rivera

Departamento: Química

El material altamente energético (HEM) hexahidro-1,3,5-trinitro-s-triazina, también conocido como RDX, tiene dos polimorfos conformacionales estables a temperatura ambiente: α -RDX (conformación molecular de grupos $-\text{NO}_2$: axial-axial-ecuatorial) y β -RDX (conformación molecular de los grupos $-\text{NO}_2$: axial-axial-axial). Ambos polimorfos pueden formarse por cristalización luego de deposición sobre sustratos de acero inoxidable (SS) y oro (Au) usando metodología de Spin Coating. α -RDX es la forma cristalina más estable a temperatura ambiente y presión ambiente. Sin embargo, β -RDX, se ha informado que es más difícil de obtener en forma masiva a temperatura ambiente, se formó fácilmente. Mediciones de espectroscopía infrarroja de reflexión-absorción (RAIRS) para sustratos revestidos con RDX proporcionaron marcadores espectrales que se utilizaron para distinguir entre los polimorfos conformacionales en varias áreas superficiales (o zonas) en ambos sustratos. La espectroscopía Raman se empleó para examinar áreas pequeñas donde la intensidad es proporcional a la altura (o escalón) de las estructuras para RDX. Las características espectrales se interpretaron y clasificaron mediante el análisis de componentes principales (ACP). Los resultados de estos análisis espectrales proporcionaron una buena correlación con los valores reportados en la literatura. Se obtuvieron condiciones optimizadas para generar casi sólo

películas cristalinas β -RDX usando velocidades de rotación crecientes sobre estos sustratos. PCA también se aplicó para predecir porcentajes de polimorfos presentes en muestras experimentales.

Por otro lado, también se presentan las propiedades ópticas para las películas cristalinas del material altamente energético (HEM) previamente citado como RDX, depositado sobre sustratos de oro (Au) e acero inoxidable (SS). Las propiedades ópticas obtenidas en el presente estudio corresponden a muestras de película delgada de polimorfo predominantemente β -RDX. Las intensidades espectroscópicas infrarrojas medidas mostraron diferencias significativas en las películas cristalinas β -RDX depositadas sobre los dos sustratos con respecto a la parte real calculada del índice de refracción. Las películas cristalinas β -RDX/Au tienen una alta respuesta dinámica, que se caracteriza por el modo de estiramiento asimétrico de los grupos nitro axiales, mientras que para las películas cristalinas β -RDX/SS, la respuesta dinámica fue mediada por el $-\text{N}-\text{NO}_2$ Modo de estiramiento simétrico. Este resultado proporciona una idea de cómo el vector del campo eléctrico se propaga a través de las películas cristalinas β -RDX depositadas sobre los dos sustratos. Las aplicaciones para los resultados obtenidos sugieren la modificación de las bibliotecas espectrales basadas en espectroscopía vibracional existentes para aplicaciones de defensa y seguridad. La comprensión de los efectos del polimorfismo de HEMs resultará en el logro de límites de confianza más altos en la detección e identificación de explosivos, especialmente en trazas o cerca de niveles de traza.

Copyright © 2017

by

José L. Ruiz Caballero

The love of my wife and my sons.

I specially want to dedicate this work to the memory of **ILEANA LABOY-ACOSTA**, who, with her unconditional love, support, and care for her nephew Pablo, allowed the development of this dissertation. RIP.

ACKNOWLEDGMENTS

My most sincere gratitude goes to my advisor **Dr. Samuel P. Hernández-Rivera**, for his invaluable scientific support, guidance and friendship and for allowing me to be a part of his team.

Thanks to all my professors including **Dr. J. Aparicio-Bolaño**, **Dr. A. Santana**, **Dr. N. Mina**, and **Dr. R. Infante** for the many outstanding scientific guidance and conversations that we shared.

Thanks to **Dr. Leonardo Pacheco**, **Amanda Figueroa**, **Luis Rosas** for their unconditional support and friendship.

A special acknowledgement to all team members of **CCSD** and **CISAC**, those who worked with my research directly or indirectly.

Thanks to all the other professors specially **Dra. Carmen A. Vega** and **Dr. Luis Morell** and colleagues from the **University of Puerto Rico, Mayagüez**.

This material is based upon work supported by the U.S. Department of Homeland Security, Science and Technology Directorate, Office of University Programs, under Grant Award **2013-ST-061-ED0001**. The views and conclusions contained in this document are those of the authors and should not be interpreted as necessarily representing the official policies, either expressed or implied, of the U.S. Department of Homeland Security.

TABLE OF CONTENTS

| | <u>page</u> |
|---|-------------|
| ABSTRACT ENGLISH | ii |
| ABSTRACT SPANISH | iv |
| ACKNOWLEDGMENTS | viii |
| LIST OF TABLES | xi |
| LIST OF FIGURES | xii |
| LIST OF ABBREVIATIONS AND SYMBOLS | xvi |
| 1 Introduction | 1 |
| 1.1 MOTIVATION AND JUSTIFICATION | 1 |
| 1.2 FUNDAMENTAL BACKGROUND | 3 |
| 1.2.1 Reflection-Absorption Infrared Spectroscopy (RAIRS) | 3 |
| 1.2.2 Raman Spectroscopy | 6 |
| 1.2.3 Atomic Force Microscopy (AFM) | 7 |
| 1.2.4 Spin Coating Technology | 8 |
| 1.2.5 Principal Components Analysis (PCA) | 9 |
| 1.2.6 Optical Properties Background – Basic Maxwell Equations Review | 10 |
| 2 CHARACTERIZATION OF α- AND β-RDX POLYMORPHS IN CRYSTALLINE DEPOSITS ON STAINLESS STEEL SURFACES | 17 |
| 2.1 LITERATURE REVIEW | 17 |
| 2.2 EXPERIMENTAL | 20 |
| 2.2.1 Materials | 20 |
| 2.2.2 Substrate Preparation | 20 |
| 2.2.3 Crystal Growth by Spin Coating | 21 |
| 2.3 Instrumentation | 21 |
| 2.4 RESULTS AND DISCUSSION | 22 |
| 2.4.1 FT-IR RAIRS Spectra | 22 |
| 2.4.2 PCA of RAIRS Spectra | 23 |
| 2.4.3 PCA of Raman Spectra | 24 |
| 2.4.4 AFM | 28 |
| 2.4.5 Solvent-Mediated Transformation to α -RDX | 31 |
| 2.5 CONCLUSIONS | 32 |

| | | |
|----------|--|-----------|
| 3 | OPTICAL PROPERTIES OF β-RDX THIN FILMS DEPOSITED ON GOLD AND STAINLESS STEEL SUBSTRATES CALCULATED FROM REFLECTION-ABSORPTION INFRARED SPECTRA | 39 |
| 3.1 | LITERATURE REVIEW | 39 |
| 3.2 | EXPERIMENTAL | 42 |
| 3.2.1 | Reagents | 42 |
| 3.2.2 | Instrumentation and Experimental Setup | 43 |
| 3.2.3 | Preparation of Au Substrates | 44 |
| 3.3 | RESULTS AND DISCUSSION | 44 |
| 3.3.1 | AFM Characterization and Determination of the Surface Concentration | 44 |
| 3.3.2 | RAIRS Measurements | 48 |
| 3.3.3 | Transversal and Longitudinal Optical Vibrations | 50 |
| 3.3.4 | Calculations of the Optical Constants for RDX/Au and RDX/SS | 52 |
| 3.4 | CONCLUSIONS | 56 |
| 4 | CONCLUSIONS | 63 |
| 4.1 | GENERAL IMPLICATIONS | 63 |
| 4.2 | FUTURE WORKS | 64 |
| | APPENDICES | 66 |
| A | Supplemental Material From Chapter Two | 67 |
| B | Supplemental Material From Chapter Three | 69 |

LIST OF TABLES

| <u>Table</u> | <u>page</u> |
|---|-------------|
| 2-1 Spectral tests for the coexistence of α/β -RDX polymorphs with increase in f value. | 31 |
| 3-1 Maximum values of the refraction Index [$n(\tilde{\nu})$], extinction coefficient [$k(\tilde{\nu})$], and absorption coefficient [$\alpha(\tilde{\nu})$] for predominantly β -RDX layers deposited on Au and SS. | 54 |
| 3-2 Maximum values of $\text{Im}(\varepsilon)$ on Au and SS substrates obtained from data shown in Figures 3-4, 3-5. Calculated values of conductivity (γ) and resistivity (ρ) for predominantly β -RDX layers deposited on the two substrates studied were found using Equation 3.2. | 54 |
| 3-3 Comparison of various experimental setups and conditions used to obtain the optical properties of RDX in the MIR region. | 56 |

LIST OF FIGURES

| Figure | page |
|--|------|
| 1-1 (a) Geometrical considerations of the polarity of the incident light in the RAIRS experiments. (b) MIR fiber optic coupled grazing angle probe to cable setup. | 4 |
| 1-2 Energy diagram for Raman scattering phenomenon. | 6 |
| 2-1 RAIRS spectra of thin RDX films on SS substrates as a function of f show the appearance of the $-\text{NO}_2$ equatorial peak at higher rotational frequencies (marked by red arrows). | 23 |
| 2-2 PCA scores plot for RAIRS spectra of RDX deposited on SS substrates showing a marked difference between low f values (3k, 4k, and 5k) and high f values (6k, 7k, and 8k). | 24 |
| 2-3 Comparison of RAIRS spectra of α/β -RDX polymorphs with PC1 and PC2 of the loadings plot for the PCA model in the asymmetric stretch spectral region: 1500 to 1650 cm^{-1} | 25 |
| 2-4 Raman spectra of the RDX crystals deposited on Stainless Steel (SS) substrate at various f values. | 26 |
| 2-5 Raman spectra (638 nm) for RDX deposits examined in the CH-stretch region showing two peaks for β -RDX (4k and 6k) and three peaks for the α -RDX polymorph (3k and 7k). Acetone Raman shift signature is clearly shown at 2927 cm^{-1} | 27 |
| 2-6 Correlation between IR and Raman spectra. PC1 favors grouping β -RDX at low f values. | 28 |
| 2-7 Surface structures formed at 8k rpm: (a) topological AFM imaging, the units of the axes are in 2 micrometers by divisions; (b) height profile along white line on the surface; and (c) white light micrograph of RDX/SS with both prisms and fibers. | 29 |

| | | |
|-----|---|----|
| 2-8 | AFM imaging and analysis of the RDX dendrite fibers produced at 3k rpm: (a) topological imaging; (b) height profile of longitudinal line (white); (c) height profile of the fibers along the transversal line (yellow); and (d) fiber dimensions determined from (b) and (c). | 30 |
| 2-9 | Vibrational Raman modes of solvents and RDX: (a) fingerprint region; (b) -CH region; (c) micrograph and chemical image of Raman intensities at 887 cm^{-1} . | 32 |
| 3-1 | AFM image and analysis of predominantly β -RDX dendrite fibers (DF1 and DF2) formed at 3k rpm on Au substrates: (a) topological imaging; (b) height profile of the horizontal line (black); (c) height profile of the fibers (DF2) along the vertical line (blue); (d) fiber dimensions determined from (b) and (c). | 46 |
| 3-2 | Unpolarized RAIRS spectra of predominantly β -RDX crystalline films on (a) Au substrates (blue trace) and (b) SS substrates (red trace). Solvent modes are presented with solid arrow, and the dashed arrows represent concomitant vibrational modes of the solvent and remaining α -RDX polymorph. | 47 |
| 3-3 | Unpolarized RAIRS spectra of predominantly β -RDX crystalline films on Au substrates at two concentrations: (a) 2.00×10^{-1} M (blue line) and (b) 2.20×10^{-4} M (red line). Solvent modes are presented with solid arrows and concomitant vibrational modes between solvent and remaining α -RDX polymorph are pointed with red dashed arrows. | 48 |
| 3-4 | Permittivity (ϵ) of predominantly β -RDX crystalline films deposited on Au substrates (segmented black line). The transversal optical function is expressed as the imaginary part [$\text{Im}(\hat{\epsilon})$; red trace] and real part [$\text{Re}(\hat{\epsilon})$; blue trace] of the permittivity. | 51 |
| 3-5 | Permittivity (ϵ) of predominantly β -RDX crystalline films deposited on SS substrates (segmented black trace). The transversal optical function is expressed as the imaginary part [$\text{Im}(\hat{\epsilon})$; red trace] and real part [$\text{Re}(\hat{\epsilon})$; blue trace] of the permittivity. | 53 |
| 3-6 | Comparison of the refractive index of RDX thin films from this contribution with literature values. RDX/ZnSe-ATR (Yang et al. ²⁹ ; green trace); β -RDX/SS (blue trace); β -RDX/Au (segmented red trace). | 55 |

| | | |
|-----|--|----|
| A-1 | RAIRS spectra thin RDX films deposited on SS substrates at various incidence angles. | 67 |
| A-2 | Raman spectra for 8k rpm showing higher intensity for the prism structure than the fibers examined. | 68 |
| A-3 | Raman spectra for 3k rpm showing intensity variations depending on the structural topology of the surface. | 68 |
| B-1 | RAIRS spectra with excited with polarized light (s & p polarizations) of predominantly β -RDX crystalline films on Au substrate compared with spectra obtained with unpolarized light. Spectrum with s-polarized light is illustrated by the blue trace; spectrum acquired with p-polarized light is represented by the red trace, and spectrum with unpolarized light is shown as the green trace. | 70 |
| B-2 | RAIRS spectra excited with polarized light (s & p polarizations) of predominantly β -RDX crystalline films on SS substrate compared with spectrum obtained with unpolarized light. Spectrum acquired with s-polarized light is illustrated by blue trace; spectrum excited with p-polarized light is represented by the red trace; spectrum obtained with unpolarized light is shown as green trace. | 71 |
| B-3 | Imaginary part of the permittivity (ε) of predominantly β -RDX crystalline films deposited on (a) gold substrates, and (b) stainless steel substrates. The blue trace corresponds to the imaginary part of the inverse of permittivity ($1/\varepsilon$), and the red trace corresponds to the imaginary part of the permittivity ($\text{Im}(\varepsilon)$; secondary “y” axis). | 72 |
| B-4 | Extinction coefficient [$k(\tilde{\nu}) = \text{Im}(n(\tilde{\nu}))$] of predominantly β -RDX crystalline films deposited on Au (blue trace; principal “y” axis), and SS (red trace; secondary “y” axis). | 72 |
| B-5 | Absorption coefficient [$\alpha(\tilde{\nu})$] of predominantly β -RDX crystalline films deposited on Au (blue trace; principal “y” axis), and SS (red trace; secondary “y” axis). | 73 |

LIST OF ABBREVIATIONS AND SYMBOLS

| | |
|---|--|
| β -RDX/Au | β -RDX crystalline films on Au substrate |
| β -RDX/SS | β -RDX crystalline films on stainless steel substrate |
| γ | Optical conductivity |
| $\hat{\mu}$ | The magnetic permeability |
| $\hat{\varepsilon}$ | The complex permittivity |
| μ | The dry air flow |
| μ_0 | The permeability of free space |
| ω | Angular velocity |
| ρ | The optical resistivity. Also, it is the reciprocal of the optical conductivity |
| σ | The electrical conductivity |
| τ | Shear stress |
| $\tilde{\nu}_{\text{LO}}$ | Longitudinal optical vibration |
| $\tilde{\nu}_{\text{TO}}$ | Transversal optical vibration |
| \tilde{n} | Complex refractive index |
| ε | Permittivity of the medium |
| ε' also symbolized as $\text{Re}(\hat{\varepsilon})$ | The real part of permittivity |
| ε'' also symbolized as $\text{Im}(\hat{\varepsilon})$ | Imaginary part of permittivity |
| ε_0 | The permittivity of free space |
| \vec{E} | Electric field vector |
| f | The rotational speed or frequency (revolutions/min, rpm) |
| k | The imaginary part of the refractive index and also known as the extinction coefficient. |

| | |
|-------------------------------|--|
| n | The real part of the refractive index |
| 3k, 4k, and 5k RPM | Magnitudes: 3,000; 4,000; and 5,000 revolutions per minutes |
| AFM | Atomic Force Microscopy |
| Au | Gold substrate |
| EMR | Electromagnetic Radiation |
| FT-IR | Fourier transform IR spectroscopy |
| HEM | High Energetic Material |
| $\text{Im}(1/\hat{\epsilon})$ | The transversal optical function |
| p | The component of electric field vector \vec{E} oriented parallel to the plane of incidence |
| PCA | Principal component analysis |
| RAIRS | Reflection-absorption IR spectroscopy technique |
| RDX | Cyclic nitramine hexahydro-1,3,5-trinitro-s- triazine |
| s | The component of electric field vector \vec{E} oriented perpendicular |
| SS | Stainless steel substrate |
| UTFs | Ultrathin films |

CHAPTER 1

INTRODUCTION

1.1 MOTIVATION AND JUSTIFICATION

Over the past century, there has been a growing interest in the development of standard practices to verify minimum acceptable performance of trace explosive detectors. According to this information, many companies are working up to improve product quality, enhance safety, facilitate market access and trade, and build consumer confidence. The U.S. Department of Commerce, NIST is one of them and it is the nation's oldest physical science laboratory. Also, ASTM International, which is formerly known as the American Society for Testing and Materials (ASTM), and is a globally recognized leader in the development and delivery of international voluntary consensus standards. This study intends to expand the knowledge in this field using spin coating technology to deposit explosives samples on different substrates. The two general goals of this investigation are to develop a technology capable of produce samples and standards of HEM with controlled size and distribution to generate specimens that would reproduce real contamination; and to study surface contamination properties such as trace sample preparation methodologies using direct transfer using syringes or micropipettes. Based on these two goals, is very important to stay ahead of these institutes for many reasons: the costs of transportation would be subtracted; and besides the residence time of these toluene-HEMs on the substrates, would be more prolonged. Finally, the applications of these well-characterized samples include use in experiments that require fine control of the distribution of loadings of analytes on surfaces.

The HEM selected for this investigation was RDX. This compound is an important ingredient in military shells, bombs, landmines, grenades, demolitions operations, and underwater blasting.¹ On the other hand, as demonstrated by Thundat et al.² the residence time of an analyte (HEM) on a substrate depends on the analyte-surface interaction forces and on the physical properties of the analyte deposited on the surface. The substrates selected for the proposed workings are gold-on-silicon surface, and stainless steel plates. Additionally, spin coating technology is in general a convenient and reproducible method for applying highly uniform thin films to substrates of all kinds. Among different techniques for organic thin film deposition, the spin coating method it is very fast and use of low cost equipment.³

The United States Department of Homeland Security (DHS) is seeking new technologies to combat and/or prevent terrorist attacks. In this sense, Primera-Pedrozo et al.⁴ developed two methodologies, one using fiber optics coupled-grazing angle probe Fourier transform infrared spectroscopy, and two, infrared microscopy. These findings were used to characterize distribution of some explosives deposited on stainless steel plates. Another important contribution to DHS was from Van Neste et al.^{2,5} who described that RDX and PETN desorbs over metals, oxides, and nitriles, very slowly and stayed on a surface for days. The final aim of this dissertation is to determine the optical properties of RDX using reflection-absorption infrared (RAIRS) spectra.⁶ Having a broader knowledge of the optical constants of the material is of benefit to research methods such as laser pyrolysis, which determines decomposition chemistry, and laser-augmented combustion and ignition.⁷ IR spectroscopy is one of a few physical methods that can be used for both *in situ* studies of various processes on surface and at interfaces, and technological monitoring of thin film structures in fields such as microelectronics or optoelectronics under serial production conditions. An IR transmission spectrum is commonly used to identify the chemical structure by correlating absorption peaks with certain bonds and lattice vibrations.⁸ Moreover, RAIRS is the most sensitive optical absorption technique available for measuring low concentration

of chemical compounds adhered to surfaces such as metals.⁹ So, with this last one the optical properties of very small amounts of substance in the form of ultrathin films will be determined accurately.¹⁰

1.2 FUNDAMENTAL BACKGROUND

1.2.1 Reflection-Absorption Infrared Spectroscopy (RAIRS)

IR spectroscopy is one of a few physical methods that can be used for both *in situ* studies of various processes on surface and at interfaces, and technological monitoring of thin-film structures in fields such as microelectronics or optoelectronics under serial production conditions. RAIRS is a technique that has been proven to be a particularly powerful research tool for the study of adsorbed layers on metal surfaces. For adsorbates on metallic or any conducting film Greenler⁶ demonstrated that the absorption of IR radiation by the adsorbate overlayer is enhanced at high angles of incidence (near grazing angle) and involves only one polarization of the incident IR beam. Ten years ago, Pacheco-Londono et al.¹¹ used both fiber optics coupled-grazing angle probe Fourier transform infrared (FT-IR) spectroscopy and infrared micro spectroscopy for characterization of the distribution and form of layers of some explosives deposited on stainless steel sheets. For a description of this methodology, FTIR spectrometer is setting up with MIR fiber optic coupled grazing angle probe. The incident ray is directed to the surface 80 degrees with respect to the normal vector. Once in contact with the sample, the incident beam generates an ellipse with dimensions shown in Figure 1-1. In addition, the electric field vector of the beam may be polarized parallel or perpendicular to the normal vector.

Thin films technology play an important role in many current areas of research in science and technology, such as sub-microelectronics, optoelectronics, optics, bioscience, flotation, materials science of catalysts, sorbents, pigments, protective and passivating coatings, and sensors. Films are found to exhibit a wide variety of structures, from irregular, amorphous aggregates to monocrystalline layers. The properties of such layers, and specially the optical and electrical properties, would be expected to depend considerably on the exact form of

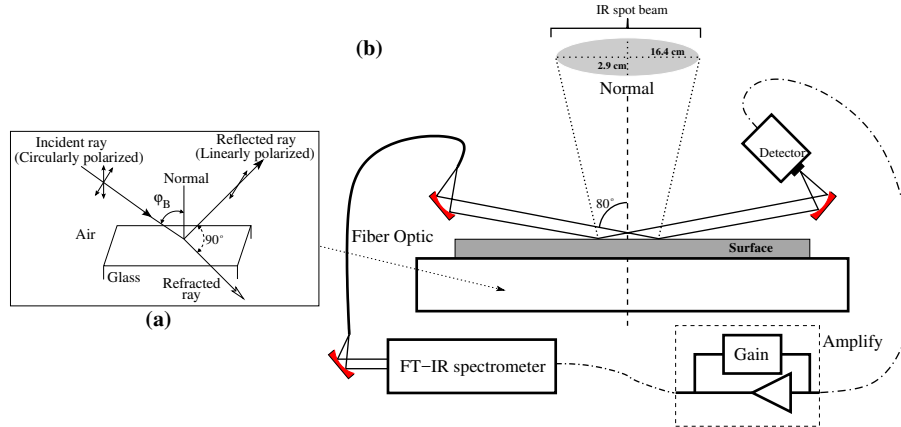


Figure 1–1: (a) Geometrical considerations of the polarity of the incident light in the RAIRS experiments. (b) MIR fiber optic coupled grazing angle probe to cable setup.

the film.¹² In principle, the determination of the amplitudes and intensities of beams of light reflected by a thin film or by a system of several films is straightforward. In principle, the optical properties of thin films can be found by setting up Maxwell's equations and applying appropriate boundary conditions. For experimental purposes, several equations have been introduced in the literature to describe the reflection from a film-covered planar interface in terms of the permittivity (ϵ) of the surrounding (immersion) medium, the film material and substrate, the thickness of the film, and the angle of incidence of the probe radiation. In spectroscopic practice, as a general rule, one measures not the absolute reflectance of a bare and coated surface, but rather the ratio of the intensities, where “s” is the component of electric field vector \vec{E} oriented perpendicular to the plane of incidence, “p” is the component of electric field vector \vec{E} oriented parallel to the plane of incidence, and “d” is the thickness of the thin-film. However, the exact analytical expressions for this ratio are cumbersome and do not allow one to discern how the optical properties of the film, the ambient media, and the substrate affect the reflectivity obtained within the framework of the thin-film approximation in terms of the so-called normalized reflectivity, or, simply, reflectivity, defined in terms of $R_0 = R(0)$ and $R = R(d)$ are the reflectances of the substrate alone and the substrate with the layer, respectively. In the case of metals, the reflectance R_0 of the substrate is close to unity, then $\frac{\Delta R}{R} \approx 1 - R$. The change in the reflectance of the

interface due to the presence of a film, is called, rather confusingly, the absorption depth:

$$\frac{\Delta R}{R} = \frac{R_0 - R}{R_0} = 1 - \frac{R}{R_0} \quad (1.1)$$

Expressions for the reflectivity are extremely tedious to evaluate by computer code, and they are not the focus of the present work. For more information, please consult the physical treatment included in Tolstoy et al.¹⁰

FT-IR spectroscopy has vast applications in this area and provides the requirements necessary to characterize both UTFs and substrates. FT-IR spectroscopy has two (2) important properties that offer practical advantages for the optical properties characterization of thin films. First, it is one of a few techniques that can be used for *in situ* studies of chemical, physical, and biological processes on surfaces and at sample interfaces.^{7,13,14} Second, it is highly useful in monitoring UTFs of adsorbates for applications in fields such as optoelectronics and microelectronics of inorganic materials.¹³ A UTF may be on the order of 100 nm (or slightly more). FT-IR spectroscopy has the sensitivity to analyze these films usually known as monolayers, and even thinner films. Finally, if FT-IR microspectroscopy itself does not provide the sensitivity to analyze thinner films, then a good alternative is to use FT-IR coupled RAIRS (FT-IR/RAIRS).⁴

To determine the optical constants using FT-IR/RAIRS, it is essential to previously obtain the following information on the experimental conditions: film thickness, relative intensity of IR absorption bands, angle of incidence of the electromagnetic radiation, and electric field vector polarization state.¹⁵ This last attribute is associated with the experiment setup and addresses the polarization of light and reflective mode in the experiments. The veracity of these suggestions is supported by the comparison of the findings of this study with those by other authors.¹⁶ Several authors have formulated several equations in which these optical constants are calculated from the boundary condition problem derived from Maxwell equations.^{6,10,17} After the exact model for an adsorbate on a highly reflective metal substrate is identified, the correct equations must be selected to solve the problem on hand.

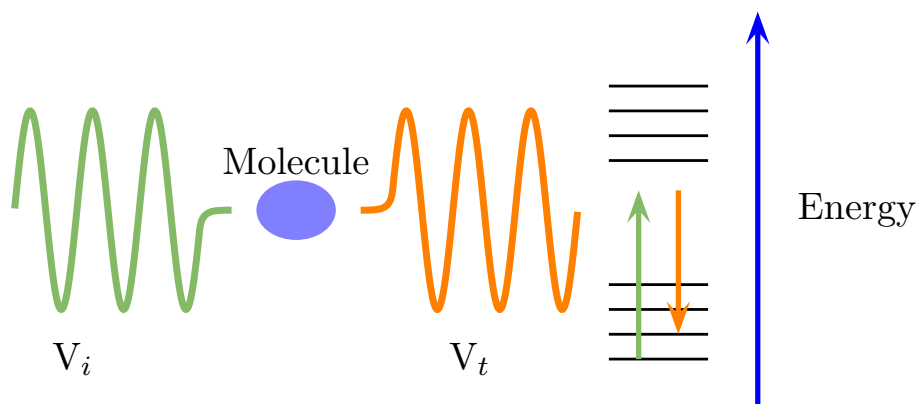


Figure 1–2: Energy diagram for Raman scattering phenomenon.

1.2.2 Raman Spectroscopy

In Raman spectroscopy, spectroscopic vibrational transitions are used to study vibrational, rotational, and other low-frequency modes in a system. It relies on inelastic scattering, of monochromatic light, usually from a laser in the visible, near infrared, or near ultraviolet portions of the electromagnetic regions (EMR). A visible photon is absorbed and then a new photon with varying frequency is emitted. This phenomenon is known as Raman scattering, as shown in Figure 1–2. When the emitted photon has the same frequency is called Rayleigh or elastic scattering.

For a vibrational mode in a molecule to be IR active, the dipole moment must change as the atoms vibrate. For a vibrational mode to be Raman active, it should induce a change in the polarizability components as the molecule vibrates. Vibrational modes can be classified into symmetric and asymmetric. Analysis of Raman polarized light can be used determine the symmetry of the band or vibrational mode. For this reason, determining the polarization of the band is an important tool in Raman spectroscopy. The ratio of intensities of the spectrum taken with parallel and perpendicular polarized light is called the depolarization ratio. If this value is from 0 to 1/3, then the band is totally symmetrical. If the depolarization ratio ranges from 1/3 to 3/4, then the band is asymmetric. In solids, some bands can produce polarization ratios greater than 3/4, and then this phenomenon is known as hyperpolarization and exclusively can be observed in solids. The vibrational

frequency for a particular mode depends on the force constant of the atoms involved in the vibration and their reduced mass. For pure or almost pure vibrations, where the vibrational mode is simply a stretch of bond that binds the atoms, the equation that is relating the force constant, mass of the atom and the frequency of vibration is show as per Equation 1.2:

$$\nu = \frac{1}{2\pi} \sqrt{F \left(\frac{1}{m_1} + \frac{1}{m_2} \right)} \quad (1.2)$$

where ν is the frequency in Hertz, F is the force constant in Newton per meter, m_1 and m_2 correspond to the mass (in kilograms) of the two atoms involved in the vibration.¹⁸

1.2.3 Atomic Force Microscopy (AFM)

An Atomic Force Microscope (AFM) is a combination of scanning tunneling microscope (STM) and a stylus profilometer. The development of AFM dates about 1986,¹⁹ and the first novelty of this technology was accompanied with contact-mode operation. In this mode, the sample surface is outlined by the bending of a cantilever that carries a sharp tip. The cantilever deflection is proportional to the force at the top of the sample, and surface profiling (topography) is made with the sharp tip kept on permanent contact with the sample even though cantilever deflection is kept constant. A good choice of the set-point deflection plays an important role for two reasons. (i) In the case for studies of soft and fragile surfaces it should be lowered but (ii) if one is interested in finding surface locations of different roughness it should be increased. With the expansion of AFM applications, the limitations of contact mode were identified, and realized that oscillatory modes help overcome this obstacle.²⁰ In this study, the technique for the examination of RDX samples prepared by spin coating was semi-contact mode. Meanwhile, AFM measurements were required to characterize the morphological aspects of the RDX crystalline deposits prepared by spin coating. In this way, a general idea of the polymorphs and its thickness can be acquired.

1.2.4 Spin Coating Technology

In this study, a methodology for growing thin crystalline films by spin coating²¹ was developed, where the α/β -RDX polymorph distribution was biased by increasing the angular velocity (ω) of deposition coating at room temperature and atmospheric pressure. The explanation for this behavior lies in the theories of spin coating, as well as the theory of creating a metastable polymorph. Spin coating is governed by the magnitude of shear stress (τ) applied to the deposited solution at increasing ω values.²¹ Most of the solution is instantly ejected during this process, where the air flow on top of the substrate applies the τ , which increases by increasing ω according to the following equation²¹

$$\tau_{r,z} = \frac{1}{2}\omega^{3/2}v_{\text{air}}^{1/2}\mu_{\text{air}}^{-1/2} = \frac{1}{2}\left[\left(\frac{60}{2\pi}\right)f\right]^{3/2}v_{\text{air}}^{1/2}\mu_{\text{air}}^{-1/2} \quad (1.3)$$

where τ is represented in planar polar coordinates (r, z) , v is the viscosity of air, f is the rotational speed or frequency (revolutions/min, rpm), and μ represents the dry air flow as controlled by the spin-coater. The aforementioned equation states that shearing stress depends on viscosity and surface tension of the solvent, as well as the rotational speed applied. This equation agrees with Stranski-Krastanov growth, since it relies on the formation of a solid skin on the surface due to an increased solvent evaporation process with the spin coating method. In addition, Capes and Cameron discussed the parameters to form a metastable polymorph in lieu of the room stable form of paracetamol: seeding of a saturated solution, obtaining the metastable form from the melting process, and isolating and drying the crystals removing as much remaining solvent as possible.²² Therefore, a qualitative hypothesis for this method would explain that the particle size and height of the film decreases while increasing f , which can also imply that lower sample concentration would be present.

1.2.5 Principal Components Analysis (PCA)

Principal component analysis (PCA) is one of the most frequently used multivariate analysis techniques for chemometric in a broad range of industrial and research applications.²³ PCA is predominantly used for evaluating sources of variation within a data set. These variations may be easily distinguished in the original data, or they may not be as obvious to the analyst. The main purpose of applying PCA in the analysis of FT-IR spectra is to classify the changes in the vibrational signatures of the compounds of interest in an organized manner, via a graphical representation called scores plot or principal components (PCs) plot.²³ The changes obtained could be due to shifts in maximum wavenumber location, a decrease in relative intensity of the bands, or the emergence or disappearance of signals, among others. The first PC contains the highest variance and the following PCs decrease in percentage of the variance captured. This variance can be examined using an orthogonal projection of the original data in the form of PCs, when these are plotted as scores.²⁴ A simple example to determine if the PCs do not express correlation is the capture of spectral noise or any other type of interference.²⁴ Consequently, these factors can be visualized in the scores plot or PC plot (PC1 vs PC2, for example), where a noisy PC spectrum may indicate the presence of interferences from ambient conditions (carbon dioxide, water vapor, or contaminants) in FT-IR spectroscopic data. In this case, preprocessing routines can be applied to the data prior to performing the multivariate analyses. If little or no spectral noise were present, preprocessing options would be unnecessary, resulting in a faster for the spectral analysis in obtaining good results and the corresponding scores plots. These plots are important because they allow the analyst to extract additional information from these data and formulate tools to explain why certain properties extracted as classes from the original spectra are alike or different. When dealing with vibrational spectra, the PCs can be compared to a ground truth by adding a reference spectrum of the sample to the original spectra used in the PCA regression to determine where the variations originate.

1.2.6 Optical Properties Background – Basic Maxwell Equations Review

The theoretical foundations to determine the optical properties of layers are based on Maxwells theory of electromagnetic radiation (EMR) of 1864.²⁵ Tolstoy, Chernyshova, and Skryshevsky¹⁰ reformulated many equations that were used in this work. The approach focuses on the macroscopic property known as the permittivity of the medium (denoted as $\hat{\epsilon}$) to explain light phenomena such as propagation, absorption, reflection, and emission in matter.²⁶ The approach describes the collective excitations of the surface depending on the EMR source.^{27,28} In this work, we adopt four premises. First, the vibrational modes of matter are excited in the IR region of the EMR spectrum. Second, because the magnetic permeability ($\hat{\mu}$) is practically zero in the optical frequencies of the IR window, the magnetic field vector (\vec{B}) can be considered as turned off because the interactions with the magnetic dipoles at these low frequencies are very small. Third, the medium considered hereby is the absorbent material. Finally, β -RDX crystalline films are isotropic. In addition, if the optical wave field is small compared to the electric field inside the atoms, it can be shown that the permittivity is independent of the magnitude of the electric field. A material that is exposed to an electric field vector \vec{E} can be polarized by placing a polarizing plate in the path of the IR beam, thereby selecting two polarization states: parallel and perpendicular electric field orientations with respect to the plane of incidence of the light. Therefore, an electric displacement \vec{D} is generated, which can be expressed as:²⁸

$$\vec{D} = \epsilon_0 \vec{E} + \vec{P} = \hat{\epsilon} \vec{E} \quad (1.4)$$

where \vec{P} is the electric polarization of the medium (also known as the net dipole moment per unit volume), which is better to define in terms of the induced dipole moment of one atom (\vec{p}_i) as $\vec{P} = \sum_i \vec{p}_i = N\vec{p}$. In other words, all densities of N atoms (molecular density) have dipole moments \vec{p} , which contribute to the total \vec{P} in a unit of volume. If we assume that the EMR propagates through the homogeneous and isotropic medium (absorbent layer), the

time-dependent wave equation can be expressed as:¹⁰

$$\nabla^2 \vec{E} - \varepsilon_0 \hat{\varepsilon} \mu_0 \hat{\mu} \frac{\partial^2 \vec{E}}{\partial t^2} - \mu_0 \hat{\mu} \sigma \frac{\partial \vec{E}}{\partial t} = 0 \quad (1.5)$$

where ε_0 is the permittivity of free space, μ_0 is the permeability of free space, $\hat{\mu}$ is the magnetic permeability, and

$$\sigma$$

is the electrical conductivity. For isotropic materials, these physical quantities can be considered scalar, but in general, they are second-rank tensors for non-isotropic materials. The solution of the above time-dependent wave equation, neglecting $\hat{\mu}$ due to the reason already explained is:

$$\vec{E} = E_0 e^{i[\omega t - (\frac{2\pi}{\lambda} n) \vec{s} \cdot \vec{r}]} e^{-\left(\frac{2\pi}{\lambda} k\right) \vec{s} \cdot \vec{r}} \quad (1.6)$$

Assuming a complex form for the solution to this equation that relates the fields in the well-known Maxwell equations, invoke the Causality Principle for the constitutive relation, integrate with respect to time, and take the Fourier transform to obtain:

$$\vec{k} = \vec{k}' - i\vec{k}'' = \hat{k} \vec{s} = (k' - ik'') \vec{s} \quad (1.6a)$$

$$\hat{n} = n - ik \quad (1.6b)$$

$$\hat{\varepsilon} = \varepsilon' - i\varepsilon'' \quad (1.6c)$$

Here, the wave vector (k) has a real part k' , which is also termed $\text{Re}(k)$, and an imaginary part k'' , which is also termed $\text{Im}(k)$. \vec{k} is expressed in terms of wavenumbers with unit vector (\hat{k}) along the direction of propagation (\vec{s}) of the wave. In this notation, the wavenumber has a real part (k') that describes the wave phase velocity in the medium, and k'' is the imaginary part of the wave vector. k'' is related to the EMR attenuation along the direction of propagation. There are two different aspects here. With respect to Equation 1.6b, the generalized complex refractive index (\hat{n}) can be expressed in terms of n , which is the real part of the refractive index, and k , which is the imaginary part of the refractive

index and also known as the extinction coefficient. This last property describes absorption phenomena and is also known as the absorption index α . Finally, the complex permittivity $\hat{\varepsilon}$ can be expressed in terms of the real part ε' and imaginary part ε'' .

If we rearrange ε' and ε'' , these equations¹⁰ results in:

$$\varepsilon' = n^2 - k^2 \quad (1.6d)$$

$$\varepsilon'' = 2nk \quad (1.6e)$$

The inverse transformation of these equations is experimentally convenient:

$$n = \sqrt{\frac{1}{2} \left[\left(\sqrt{(\varepsilon')^2 + (\varepsilon'')^2} \right) + \varepsilon' \right]} \quad (1.7)$$

$$k = \sqrt{\frac{1}{2} \left[\left(\sqrt{(\varepsilon')^2 + (\varepsilon'')^2} \right) - \varepsilon' \right]} \quad (1.8)$$

The Beer-Lambert-Bouguer (BLB) law expresses a relationship among the decay constant (absorption coefficient, α), k'' , ε'' , and extinction coefficient k :

$$\alpha = 2k = \left(\frac{4\pi}{\lambda} \right) k = \frac{2k\omega}{c} = \frac{\varepsilon''\omega}{cn} \quad (1.9)$$

When the light is attenuated, the real part of the permittivity ε' is determined by:

$$\text{Im} \left(\frac{1}{\hat{\varepsilon}} \right) = \frac{\varepsilon''}{(\varepsilon')^2 + (\varepsilon'')^2} \quad (1.10)$$

Solving this equation for ε' results in:

$$\varepsilon'(\tilde{\nu}) = \sqrt{\frac{\varepsilon''(\tilde{\nu})}{\text{Im} \left(\frac{1}{\hat{\varepsilon}} \right)} - \varepsilon''(\tilde{\nu})} \quad (1.11)$$

Yamamoto and Ishida²⁹ refer to functions $\text{Im} \left(\frac{1}{\hat{\varepsilon}} \right)$ and $\text{Im}(\hat{\varepsilon}) = \varepsilon''$ as the transverse optical function and longitudinal optical function, respectively. The peak maximum of the function $\text{Im}(\hat{\varepsilon})$ vs. $\tilde{\nu}$ corresponds to $\tilde{\nu}_{TO}$, whereas the maximum of $\text{Im} \left(\frac{1}{\hat{\varepsilon}} \right)$ corresponds to $\tilde{\nu}_{LO}$ vibrations of the medium. In conclusion, every optical equation is expressed as a function

of the real part of the permittivity (ε'), imaginary part of the permittivity ($\text{Im}(\hat{\varepsilon}) = \varepsilon''$), and imaginary part of the inverse of the permittivity ($\text{Im}\left(\frac{1}{\hat{\varepsilon}}\right)$).

Yamamoto and Ishida²⁹ and Tolstoy, Chernyshova, and Skryshevsky¹⁰ express a relationship among the imaginary part of the permittivity (and its inverse), thickness (d), EMR incidence angle (φ_1), IR wavenumber $\tilde{\nu}$ (cm^{-1}), and relative intensity of the reflected IR signal ($\frac{\Delta R}{R}$) as follows:

$$\text{Im}\left(\frac{1}{\hat{\varepsilon}}\right) = \frac{\left(\frac{\Delta R}{R}\right)_p}{8\pi d\tilde{\nu} \sin(\varphi_1) \tan(\varphi_1)} \quad (1.12)$$

$$\text{Im}(\hat{\varepsilon}) = \frac{\left(\frac{\Delta R}{R}\right)_s}{8\pi d\tilde{\nu} \cos(\varphi_1)} \quad (1.13)$$

where the subscript “s” (“senkrecht” or perpendicular) indicates that the incident light is polarized at 90° with respect to the normal plane of incidence, denoted perpendicular polarization. The subscript “p” denotes parallel polarization (or p-polarization) and represents light polarized at 0° with respect to the normal plane of incidence. The control of these states of polarizations is very important for the experimental setup proposed herein.³⁰ Because the EMR intensity is proportional to the square of \vec{E} (electric field strength), the ratio $\frac{\Delta R}{R}$ measures the reflectance change (ΔR) of the thin film deposited on the substrate with respect to the reflectance due to a clean substrate. It is important to emphasize that $\left(\frac{\Delta R}{R}\right)_s$ is inversely proportional to the angle of incidence, whereas $\left(\frac{\Delta R}{R}\right)_p$ has maximum values at grazing angles of incidence.

REFERENCE LIST

- [1] G. Hugh, R. Gallaher, M. Vrcelj, and J. N. Sherwood. The crystal growth and perfection of 2,4,6-trinitrotoluene. *J. Cryst. Growth.*, pages 486–498, 2003.
- [2] C. W. Van Neste, L.R. Senesac, and T. Thundat. Standoff spectroscopy of surface adsorbed chemicals. *Anal. Chem.*, 81:1952–1956, 2009.
- [3] S. Panigrahi, S. Waugh, S.K. Rout, A.K. Hassan, and A.K. Ray. Study of spin coated organic thin film under spectrophotometer. *Ind. J. Phys.*, 78(8):823–826, 2004.
- [4] O. Primera-Pedrozo, Y. Soto-Feliciano, L. Pacheco-Londoño, and S. Hernández-Rivera. Detection of high explosives using reflection absorption infrared spectroscopy with fiber coupled grazing angle probe/ftir. *Sensing and imaging. An International Journal.*, 10(1):1–13, 2009.
- [5] L.A. Pinnaduwegea, T. Thundata, A. Gehla, S.D. Wilsona, D.L. Heddena, and R.T. Lareaub. Desorption characteristics of uncoated silicon microcantilever surfaces for explosive and common nonexplosive vapors. *Ultramicroscopy.*, 100:211–216, 2004.
- [6] R.G. Greenler. Infrared study of absorbed molecules on metal surfaces by reflection techniques. *J. Chem. Phys.*, 44:310–314, 1996.
- [7] R.A. Isbell and M.Q. Brewster. Optical properties of energetic materials: Rdx, hmx, ap, nc/ng, and htpb. *Propellants, Explosives, Pyrotechnics.*, 23:218–224, 1998.
- [8] R.A. Isbell and M.Q. Brewster. Optical properties of rdx and hmx. *MRS Proceedings.*, 418:85–90, 1995.
- [9] Y. Soto-Feliciano, O.M. Primera-Pedrozo, L. Pacheco-Londoño, and S.P. Hernandez-Rivera. Temperature dependence of detection limits of tnt on metallic surfaces using fiber optic coupled ftir. *Proc. SPIE*, 6201:62012H–62012H–9, 2006. doi: 10.1117/12.665897.

- [10] V.P. Tolstoy, V.A. Chernyshova, and V.P. Skryshevsky. *Handbook of infrared spectroscopy of ultrathin films*. John Wiley & Sons, Inc., Hoboken, NJ., 2003. ISBN: 9780471234326.
- [11] L. Pacheco-Londoño, A. Santiago, J. Pujols, O.M. Primera-Pedrozo, A. Mattei, W. Ortiz, O. Ruiz, M. Ramirez, and S.P. Hernández-Rivera. Characterization of layers of tetryl, tnbn and hmx on metal surfaces using fiber optics coupled grazing angle-ftir. *Proc. SPIE.*, 6542:65423K–65423K–10, 2007. doi: 10.1117/12.720976.
- [12] J.D. Cockcroft. On phenomena occurring in the condensation of molecular streams on surfaces. *Proc. R. Soc. London, Ser. A.*, 119(782):293–312, 1928.
- [13] D.L. Allara, A. Baca, and C.A. Pryde. Distortions of band shapes in external reflection infrared spectra of thin polymer films on metal substrates. *Macromolecules.*, 11(6):1215–1220, 1978.
- [14] O.S. Heavens. Thin film research today. *Nature*, 228(5276):1036–1039, 1970.
- [15] R.G. Greenler, R.R. Rahn, and J.P. Schwartz. The effect of index of refraction on the position, shape, and intensity of infrared bands in reflection-absorption spectra. *J. Catal.*, 23(1):42–48, 1971.
- [16] C.S. Yang, B.R. Williams, A. Tripathi, M.S. Hulet, A.C. Samuels, J.A. Domanico, J. May, R.W. Miles Jr, and A.W. Fountain III. Spectral characterization of rdx, etn, petn, tatp, hmted, hmx, and c-4 in the mid-infrared region. (no. ecbc-tr-1243). Technical report, DTIC Document, Maryland, 2014. U.S. Army Edgewood Chemical Biological Center: Aberdeen Proving Ground.
- [17] P.B. Johnson and R.W. Christy. Optical constants of the noble metals. *Phys. Rev. B.*, 6(12):4370, 1972.
- [18] C. Raman and Krishnan K. A new type of secondary radiation. *Nature*, 121:501–502, 1928.
- [19] G. Binnig, C. Quate, and Ch. Gerber. Atomic force microscope. *Phys. Rev. Lett.*, 56:930–934, 1986.

- [20] K. Boussua, B. Van der Bruggena, A. Volodinb, J. Snauwaertb, C. Van Haesendonckb, and C. Vandecasteelea. Roughness and hydrophobicity studies of nanofiltration membranes using different modes of afm. *J. Colloid Interface Sci.*, 286(2):632–638, 2005.
- [21] N. Sahu, B. Parija, and S. Panigrahi. Fundamental understanding and modeling of spin coating process: A review. *Ind. J. Phys.*, 83:493–502, 2009.
- [22] J.S. Capes and R.E. Cameron. Effect of polymer addition on the contact line crystallisation of paracetamol. *Cryst. Eng. Comm.*, 9:84–90, 2007.
- [23] R.G. Brereton. *Applied Chemometrics for Scientists*. John Wiley & Sons, Inc., New York, NY., 2007. ISBN: 978-0-470-05777-3.
- [24] K.H. Esbensen, D. Guyot, F. Westad, and L.P. Houmoller. *Introduction to Multivariate Data Analysis - Overview*. In *Multivariate Data Analysis: in Practice*. Multivariate Data Analysis, Oslo, Norway, 5th edition, 2004. ISBN-13: 978-8299333030.
- [25] J.C. Maxwell. *A Treatise on Electricity and Magnetism Unabridged.*, volume one. Dover Publication, Inc., New York, NY., 3th edition, 1954. ISBN: 486-60636-8.
- [26] K. Yamamoto and H. Ishida. Optical theory applied to infrared spectroscopy. *Vib. spectrosc.*, 8(1):1–36, 1994.
- [27] C. Kittel. *Introduction to Solid State Physics*. John Wiley & Sons, Inc., Danves, MA., eighth edition, 2005. ISBN : 978-0-471-41526-8.
- [28] N.W. Ashcroft and N.D. Mermin. *Solid state physics*. Holt, Rinehart and Winston, New York, NY, 1976. ISBN: 0-03-083993-9.
- [29] K. Yamamoto and H. Ishida. Interpretation of reflection and transmission spectra for thin films: Reflection. *Appl. Spectrosc.*, 48(7):775–787, 1994.
- [30] K. Yamamoto and H. Ishida. Optical theory applied to infrared spectroscopy. *Vib. spectrosc.*, 8(1):1–36, 1994.

CHAPTER 2

CHARACTERIZATION OF α - AND β -RDX POLYMORPHS IN CRYSTALLINE DEPOSITS ON STAINLESS STEEL SURFACES

Published in: *Journal of Crystal Growth and Design*. 16(7) (2016) 3631-3638. Amanda M. Figueroa-Navedo, Jose L. Ruiz-Caballero, Leonardo C. Pacheco-Londoño, and Samuel P. Hernandez-Rivera. DOI: [10.1021/acs.cgd.6b00078](https://doi.org/10.1021/acs.cgd.6b00078)

2.1 LITERATURE REVIEW

The highly energetic material (HEM) studied in this work was the cyclic nitramine hexahydro-1,3,5-trinitro-s-triazine, which is commonly known as cyclonite or Research Department Explosive (RDX). This HEM is classified as a secondary explosive, and it is widely used in military applications as one of the main ingredients of plastic bonded explosives (PBX: Semtex, C2, C3, and C4), and other explosives formulations. RDX has been widely studied in its room temperature stable crystalline α -polymorphic form (α -RDX). However, several studies discuss the characterization of the β -metastable form of RDX (β -RDX) under standard growth conditions, which involve drop-casting techniques at room temperature and atmospheric pressure.¹⁻⁵ The formation of β -RDX follows Ostwalds step rule, where the least stable polymorph is formed first due to a very small change in Gibbs free energy between both crystalline forms.⁶ This rule states that kinetics takes a prominent role over thermodynamics and that the kinetically favored species is formed first.^{7,8} Concentrations below the solubility parameters increases the probability of obtaining the metastable form. Therefore, it has proven difficult to obtain only β -RDX without simultaneous formation of α -RDX on the substrate of interest, because there is very little change

in the rates of formation of these polymorphs.¹ Nevertheless, the β -RDX polymorph was obtained with drop-cast crystallization studies by Goldberg and Swift, who demonstrated consistent growth of β -RDX on glass substrates using various solvents.¹ Mercado et al. studied the characterization of RDX nanoparticles deposited by an aerosol jet technique, where they also found the coexistence of room temperature phases of RDX (β and α).⁹ Spectroscopic measurements of the polymorphic forms of RDX have been used to follow its transition from α -RDX using temperature,¹⁰ concentration,¹¹ mechanical contact,^{2,3,5,12-14} and specific solvent crystallization.^{1,14} Polymorphism within energetic materials (both primary and secondary) is a main cause of concern for trace detection and quantification due to the change in physical properties inherent to polymorphism.

Various studies on the polymorphism of RDX show that there are five phases: α , β , γ , δ , and ε .^{2-5,13-18} Of these five forms, only α -RDX and β -RDX exist at room temperature and ambient pressure. In the α -RDX crystalline form, the orientations involving two of the $-\text{NO}_2$ groups are in axial positions and the third group is in an equatorial position (AAE), imparting C_S symmetry for the molecular conformer when in its static equilibrium position. However, in the β -RDX polymorph, the orientations of the three $-\text{NO}_2$ groups are all axial (AAA), leading to a higher symmetry (C_{3V}) for its equilibrium conformation. Regarding crystal morphology, Hultgren first described α -RDX crystals as orthorhombic.¹⁹ In contrast, McCrone described the β -polymorph as needle-like.¹⁵ Using IR vibrational spectroscopy, Karpowicz demonstrated that RDX assumes an (AAA) conformation in both liquid solution and its vapor phase, but that the room temperature bulk solid phase assumed the (AAE) conformation in crystalline form.¹⁶ More recent studies by Torres et al. described the β -polymorph as structures resembling islands as well as scattered particles.¹¹ They described the α -RDX polymorph as well defined crystals. In contrast, Goldberg and Swift described both α/β -RDX polymorphs as assuming a variety of different morphologies.¹

To investigate these apparent contradictions, it is important to use basic aspects of nucleation theories. An ideal thin film growth on a surface involves smooth, layered growth

throughout the surface. This two-dimensional (2D) growth is called Frank-van der Merwe mode. The growth of 3D islands throughout the surface is called Volmer-Weber mode. There is a third type of growth, called Stranski-Krastanov mode, that implies a wetting monolayer below the 3D structures.²⁰ One possible explanation for the formation of Volmer-Weber mode structures originates from mass transfer limitations, where a major challenge in shearing solution is the prevention of crystal defects, which often plays a major role in void formation and dendritic growth.^{7,8} The formation of islands with defined void centers provides indication of abrupt growth.²¹ Evidence of possible Stranski-Krastanov nucleation has been reported by atomic force microscopy (AFM) measurements for dihexylterthiophene (DH3T), which exhibited island-like structures.²² However, this evidence to support this type of growth mechanism has been highly debated.²¹⁻²³ AFM measurements are required to characterize the morphological aspects of the films prepared where a general idea of the polymorphs within the substrate is known. However, AFM measurements can provide evidence of Stranski-Krastanov growth if a monolayer or thin film is present.¹⁷ Furthermore, Raman spectra should confirm polymorphism in small areas of the structures generated. In contrast, Fourier transform infrared (FT-IR) spectroscopy should allow assessment of larger sample areas. Therefore, RDX conformational polymorphs within these crystal structures can be discovered by FT-IR measurements and confirmed by Raman spectra. In this work, the area studied by FT-IR was > 3,000 times larger than the area studied by Raman microspectroscopy. Thermal Raman microspectroscopy was used to study drug polymorphism and is commonly used in the pharmaceutical industry.^{24,25} An important aspect of this study involved the methodology developed for samples preparation since these were needed to address the required morphological AFM evidence for the presence of thin films. Various thermal inkjet methodologies have provided major advances in the control of morphology and polymorphism within thin films.^{20,26}

2.2 EXPERIMENTAL

2.2.1 Materials

The solvents used in this work: acetone (CH_3COCH_3 , 98% w/w), methanol (HPLC grade), and isopropyl alcohol (IPA, 99% w/w), were purchased from Sigma-Aldrich Chemical Co. (Milwaukee, WI, USA) and used without further purification. Water used was doubly distilled and deionized (18.0 M ohms) to render it equivalent to HPLC grade water. RDX was synthesized according to the Bachmann method with minor modifications.²⁷ Stainless steel (SS) substrates ($1.0 \times 1.0 \text{ in}^2$) were purchased from Stainless Supply, Inc. (Monroe, NC, USA).

2.2.2 Substrate Preparation

The substrates were cleaned by sonication in acetone followed by rinsing with distilled water and IPA. Once the substrates were cleaned, vibrational chemical maps using Raman microspectroscopy (InVia, 532 nm; Renishaw, Inc., Hoffman Estates, IL, USA) were obtained to determine the degree of cleanliness of the substrates surfaces. The chemical maps of the substrates showed that these evidenced: (a) no presence of RDX; and (b) no solvent remaining after the drying process. The RDX coatings on hydrophobic SS substrates (RDX/SS) were prepared from concentrated stock solutions of approximately 0.2 M RDX in acetone (working solution), according to the methodology discussed by Hikal where homogeneity on quartz substrates was established.²⁸ This solvent choice did not necessarily guaranteed that homogeneity would persist on the hydrophobic SS substrates. Various previously reported RDX deposition methods have used metallic substrates for samples and standards preparation as well as for fundamental studies.²⁹⁻³¹ Dilute solutions of 49 ppm (mg L^{-1}) were prepared from the working solution to evaluate the reported findings on the influence of analyte concentration on the occurrence of polymorphism in RDX.⁷

2.2.3 Crystal Growth by Spin Coating

A model 6800 spin coater system (Specialty Coating Systems, Inc., Indianapolis, IN, USA) was used to develop the methodology for RDX deposition on SS substrates. Depositions on the substrates were made at 20°C and for f values from 3k to 8k rpm at 1k rpm increments. The ramp increase time, dwell time, and ramp decrease time were set at 2, 60, and 5 s, respectively. The interior of the spin coater chamber was purged from dust particles by filtered dry air. Six substrates and replicas were prepared by depositing 100 μL of the working RDX solution on various SS substrates by spin coating using as f was gradually increased.

2.3 Instrumentation

FT-IR spectra were recorded on an evacuable benchtop interferometer (IFS-66 v/s, Bruker Optics, Billerica, MA, USA) equipped with a DTGS detector and a KBr beamsplitter with the aid of a reflection accessory (A-513/Q, Bruker Optics) in which the angle of incidence could be varied from: 13° to 85°. FT-IR spectral data were acquired and analyzed using OPUSTM software suite (v. 7.2.139.1294, Bruker Optics). The optimum incidence angle chosen for RAIRS depends on the type of metal where the analyte is adsorbed.³² The grazing angle is the value of the incidence angle where the intensity of reflected light increases the most with respect to a phase change (δ) when using polarized light parallel and perpendicular to the substrate.³² All measurements were made at an angle of incidence of 80°, which although it is not the optimum incidence angle for reflectance-absorption infrared spectroscopy (RAIRS) measurements as seen in Appendix A, Figure A-1, it was a much more convenient and reproducible value. The reference spectra which included the β -RDX spectra used for the last section of this study were also carried out at 80° incidence.³¹ The interferograms were collected at a 4 cm^{-1} nominal spectral resolution. Sample areas of 1.0 \times 1.0 in^2 were analyzed in RAIRS mode in the spectral range 400–1600 cm^{-1} with 32 background and sample scans and a scanner velocity set to 4.0 kHz.

Raman spectra of the various crystal structures formed on the SS surface were obtained using a Raman microspectrometer (RM2000; Renishaw, Inc.) equipped with a Leica DM/LM microscope (100X objective) in the 100–3200 cm^{-1} region. The spectral parameters included 10 s scans with 8 accumulations per measurement. A 632 nm laser (Melles-Griot, IDEX Corp., Carlsbad, CA, USA) was employed as the excitation source with a power of 0.23 mW reaching the sample. The laser beam diameter was measured at 5.2 m with the 100X objective. Mapping measurements were made in an model Xplora Raman microspectrometer (Horiba Jobin-Yvon SAS, Edison, NJ, USA) using a CCD detector, 100X objective and a 638 nm solid state diode as the laser excitation source with 1.10 mW of laser power at the sample. These spectral parameters included 10 s scans with 3 accumulations and 9 μm of linear scan area with steps of 2 μm . An AFM (model CP-II; Veeco Instruments, Inc., Plainview, NJ, USA) was employed to characterize the morphology and topology of the coatings prepared. The cantilever was used in non-contact mode with a natural frequency of 75.5 kHz. The imaging software, Image Processing and Data Analysis Software, v. 2.1.15 (Veeco Instruments, Inc.) provided with this equipment was employed for roughness calculations.

2.4 RESULTS AND DISCUSSION

2.4.1 FT-IR RAIRS Spectra

Representative RAIRS spectra of thin RDX films on highly polished SS substrates prepared by spin coating at increasing f values are shown in Figure 2–1. The main differences observed between the two RDX phases present were the spectral markers related to the position of one of the $-\text{NO}_2$ groups. The prominent feature corresponding to the asymmetric $-\text{NO}_2$ stretch in β -RDX is the broad peak that appears in the 1592-1600 cm^{-1} region. However, for α -RDX, this prominent peak unfolds into additional peaks, 1535 cm^{-1} (tentatively assigned to $\nu_{\text{as}} \text{NO}_2^{\text{eq}}$ asymmetric stretch in α -RDX), 1581 and 1582 cm^{-1} (tentatively assigned as $\nu_{\text{as}} \text{NO}_2^{\text{ax}}$ asymmetric stretch in α -RDX; 1600 cm^{-1} in β -RDX). These vibrational modes assignments are based on the values reported by Millar *et al.*², Dreger and Gupta,⁴

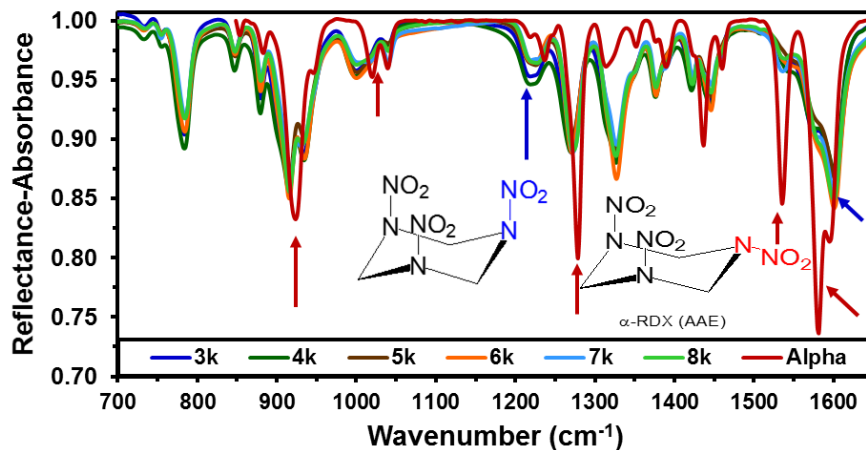


Figure 2–1: RAIRS spectra of thin RDX films on SS substrates as a function of f show the appearance of the $-\text{NO}_2$ equatorial peak at higher rotational frequencies (marked by red arrows).

and Infante-Castillo et al.^{10,33} Other prominent vibrational modes at 1279 cm^{-1} (tentatively assigned as $\nu\text{N-N-O}_2$ stretch in α -RDX; 1270 cm^{-1} β -RDX), 1390 cm^{-1} (tentatively assigned as $\gamma\text{-CH}_2$ out of plane bending in α -RDX; 1377 cm^{-1} in β -RDX), 1535 cm^{-1} (tentatively assigned as $\nu_{\text{as}}\text{NO}_2^{\text{eq}}$ asymmetric stretch in α -RDX) are also present. These spectra were compared to a reference standard obtained from a deposition of the 0.2 M RDX solution that formed only the α -polymorph (labeled “Alpha” in Figure 2–1). Further evidence of the coexistence of α/β -RDX phases was investigated by Raman micro spectroscopy. However, the differences in FT-IR spectra were evaluated by PCA.

2.4.2 PCA of RAIRS Spectra

The RAIRS spectral region of $1500\text{--}1650\text{ cm}^{-1}$ was used for PCA regression analysis, since this region is highly important in the spectroscopic differentiation between the two polymorphs. Figure 2–2 displays the scores plot for baseline corrected RAIRS spectra. First derivative preprocessing was applied to the spectral data to eliminate variations within the spectra for shifts in the baseline. The Figure shows the spectral variation of the RDX deposited at each f , where a general increase in f is correlated with PC2 in the multivariate analysis. PC2 also reflects a general clustering at low (3k–5k rpm) and high (6k–8k rpm) f

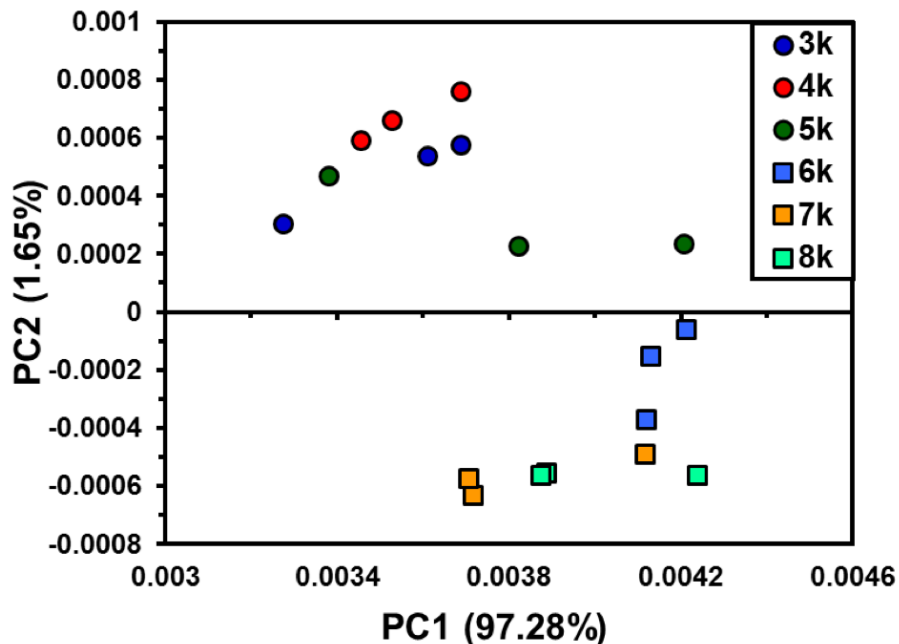


Figure 2–2: PCA scores plot for RAIRS spectra of RDX deposited on SS substrates showing a marked difference between low f values (3k, 4k, and 5k) and high f values (6k, 7k, and 8k).

values. This is indicative of a major change detected by FT-IR that differentiates these two broad classification parameters.

The spectra obtained for depositions at 7k rpm and 8k rpm point to the direction of coexistence of α/β -RDX. This was correlated with the PCA loadings plot using vibrational modes at 1039 cm^{-1} (tentatively assigned to $\nu\text{N-C-N}$), 1390 cm^{-1} (tentatively assigned as $\gamma\text{-CH}_2$ out of plane bending in α -RDX), 1437 cm^{-1} (βCH_2 in-plane bending), and 1535 cm^{-1} ($\nu_{\text{as}}\text{NO}_2^{\text{eq}}$ asymmetric stretch in α -RDX). The spectra reveal similar peaks at 1270 cm^{-1} , with no broadening of the peak ($\nu\text{N-N-O}_2$ stretch). For 6k rpm, intense bands were located at 1326 cm^{-1} ($\nu\text{N-N-O}_2$ stretch) and 1446 cm^{-1} (tentatively assigned to βCH_2 in-plane bending) compared to other f values.⁶ PC1 correlates with the increasing intensity of the axial $-\text{NO}_2$ vibrational mode, which is characteristic of the presence of β -RDX.

2.4.3 PCA of Raman Spectra

Raman micro spectroscopy is often described as a complementary tool to RAIRS mode FT-IR spectroscopy because it is able to focus on particles and structures on the micron scale

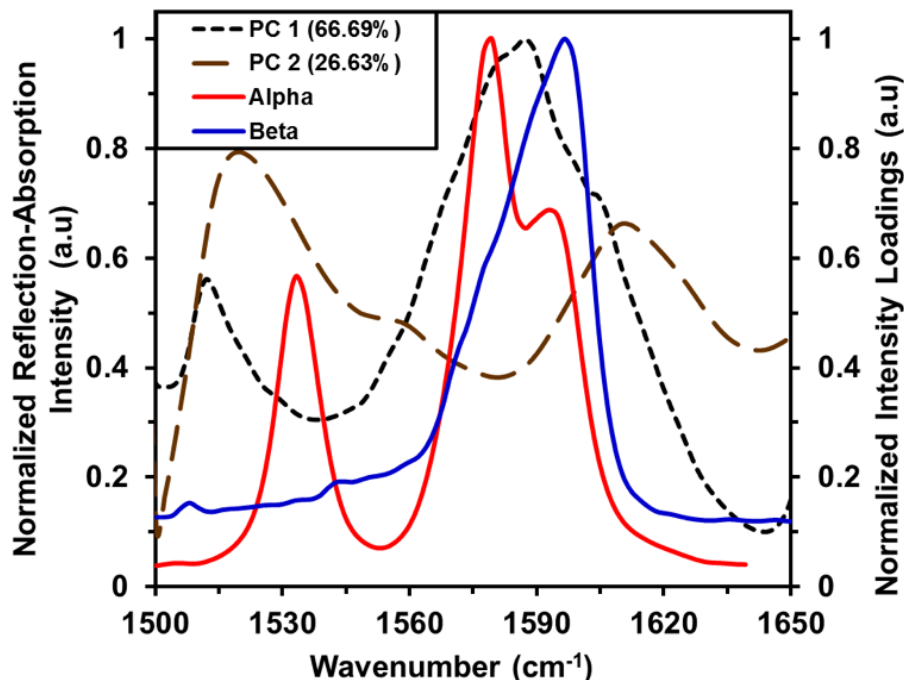


Figure 2-3: Comparison of RAIRS spectra of α/β -RDX polymorphs with PC1 and PC2 of the loadings plot for the PCA model in the asymmetric stretch spectral region: 1500 to 1650 cm^{-1} .

with higher spatial resolution. This technique was employed to examine the polymorphism of RDX within the various crystal structures detected. Raman mapping measurements were taken in steps of 2 nm to examine and confirm the presence of each polymorph on the substrates. Fiber-like structures, as well as islands and crystals (prisms), were examined for Raman activity under $100\times$ magnification. The region studied was 100–3200 cm^{-1} . A wide variation in intensities is noted in each of the colored coded spectra shown in Figure 2-4. These intensities were directly dependent on the topology of the structure examined. For more information, which it is out of the sequence of this dissertation, some variations are illustrated in the Appendix section, Figures A-2 and A-3. Spectral data were preprocessed with baseline correction to avoid affecting the PCs. Figure 2-4 shows three regions that can be used to distinguish the polymorphs: Region A: the ring breathing modes at 800–900 cm^{-1} : the most prominent spectral feature in this region corresponds to the ring-breathing

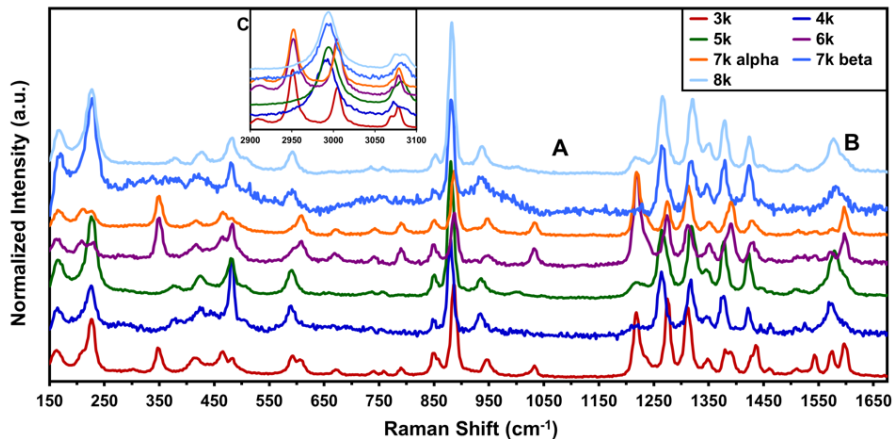


Figure 2-4: Raman spectra of the RDX crystals deposited on Stainless Steel (SS) substrate at various f values.

mode for the β -polymorph was observed at 881 cm^{-1} . The corresponding mode for the α -polymorph was located near at 866 cm^{-1} .^{10,11,33} Region B: asymmetric -N-O_2 stretch region at 1600 cm^{-1} , and Region C: CH symmetric stretch region at $2800\text{--}3050\text{ cm}^{-1}$.⁶ Notably, the spectrum at 7k rpm falls within the region of the α -RDX polymorph in Figure 2-4. In addition, another spectrum of the sample prepared at 7k rpm has to be assigned as belonging to the β conformer of RDX. Examples of RDX polymorph identification by Raman spectra are shown in Figure 2-5. One representative spectra per rpm is shown in normalized intensity values. Alpha and beta RDX spectra were found at 7k rpm and representative spectra of both polymorphs formed at 7k are shown. The α -RDX form can be recognized for the samples prepared at f values of 3k (red), 6k (violet), and 7k alpha (orange). The β -RDX form was present at depositions made at f values of 4k (navy blue), 5k (green), 7k beta (lighter blue), and 8k (sky blue). The most noticeable region for differentiating between the two polymorphs is the C-H stretch region from $2850\text{ to }3100\text{ cm}^{-1}$, where α -RDX deposits show three peaks at $2953, 3009,$ and 3081 cm^{-1} , while β -RDX shows two at 2996 and 3084 cm^{-1} . The ring-breathing mode located at 881 cm^{-1} for the β -RDX polymorph (886 cm^{-1} for the α -RDX polymorph) agree precisely with literature value.^{1,9-11,33} Furthermore, the -N-O asymmetric stretching mode shows a broad peak at 1600 cm^{-1} for the β - form, indicating the presence of slightly non-totally equivalent axial nitro group substituents.^{1,9-11,33} These

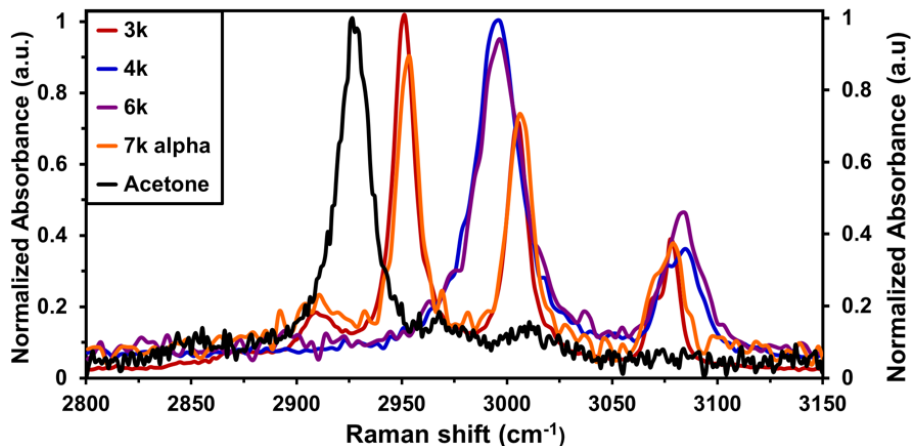


Figure 2-5: Raman spectra (638 nm) for RDX deposits examined in the CH-stretch region showing two peaks for β -RDX (4k and 6k) and three peaks for the α -RDX polymorph (3k and 7k). Acetone Raman shift signature is clearly shown at 2927 cm^{-1} .

vibrational modes have been extensively documented in the literature, and there is good agreement between our results and those of Infante-Castillo et al. and others.^{1-3,9-11,18,33} Figure 2-5 provides evidence of the presence of the solvent used for depositing the RDX samples: acetone. Evidence of the presence of acetone in α -RDX spectra in Figure 2-5, was also based on the $-\text{CH}$ vibrational marker at 2926 cm^{-1} .³⁴ Vibrational markers from the solvent (acetone) were found. These can be appreciated in Figure 2-5 after normalizing intensity values in the secondary “y” axis. Notice that an increased presence of solvent at 2927 cm^{-1} is evidence of a solvent-mediated transformation from β -RDX to α -RDX.

Raman and IR spectra were then added to the same matrix for analysis by direct standardization in the region from 1500 to 1600 cm^{-1} . To account for intensity variations within the spectra, centroid scaling, standard normal variate, and first derivative were applied as preprocessing steps to the modified matrix. The scores plot obtained after model modification is shown in Figure 2-6, where the IR and Raman spectra are correlated for f values (3k and 4k) and for high f values (5k, 6k, 7k, and 8k) with respect to PC1 for RDX. The β -RDX reference spectra at a concentration of 49 ppm was added for comparison of the $-\text{NO}_2$ vibrational mode in RAIRS. When compared to the reference IR spectra for α/β -RDX, low f values favors the β -RDX polymorph.

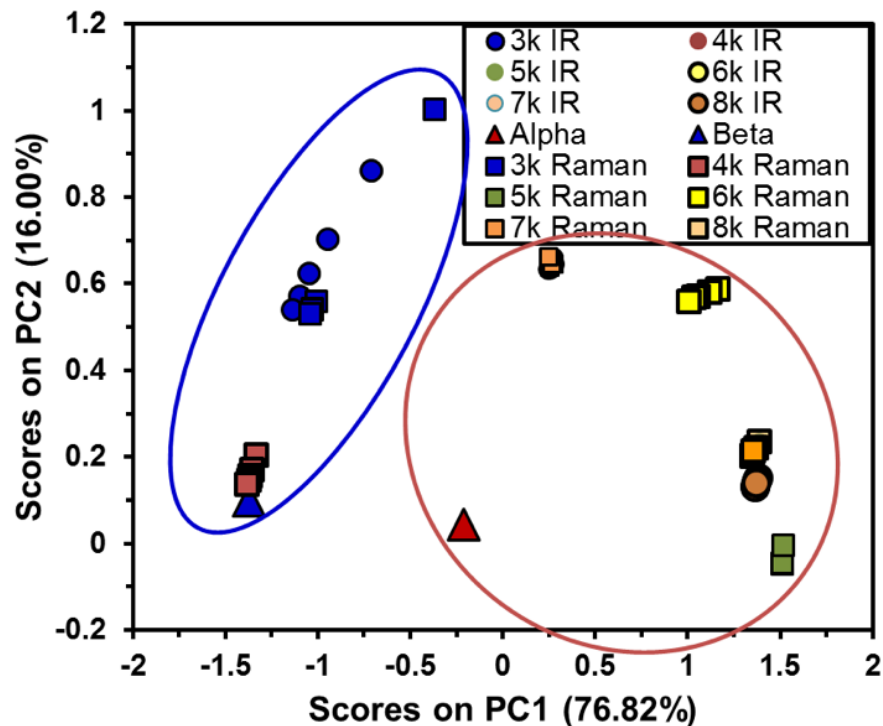


Figure 2-6: Correlation between IR and Raman spectra. PC1 favors grouping β -RDX at low f values.

2.4.4 AFM

The purpose of characterizing the RDX crystal structures formed on SS substrates by AFM was to study the surface topology and morphology for both polymorphs. The Raman spectra shown in Figures 2-4 and 2-5 show marked intensity fluctuations, before normalization. High intensities were obtained for the prism structures near the center of the substrates at 5k rpm. The next most intense Raman spectra also represented prism structures, which were near the center and the corner of the substrate at 8k rpm.

As seen in Figure 2-7, the height of these crystal structures was as high as 550 nm following deposition at 8k rpm on a $10 \times 10 \mu\text{m}^2$ region. Fiber like structures in the shape of dendrites were found for the RDX deposits at 3k, 4k, and 5k rpm (see Appendix A, Figures A-2, A-3). The RDX structures with lower intensity found on the substrates were fibers, which were found on the RDX/SS samples formed at 3k rpm (see Appendix A, Figures A-3). The characterization of the fibers deposited at 3k rpm is shown in Figure

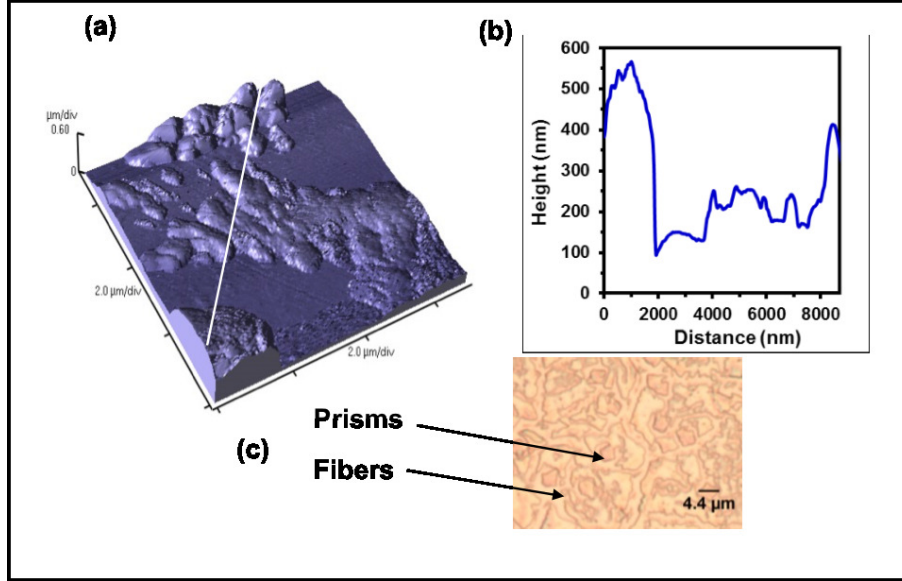


Figure 2-7: Surface structures formed at 8k rpm: (a) topological AFM imaging, the units of the axes are in 2 micrometers by divisions; (b) height profile along white line on the surface; and (c) white light micrograph of RDX/SS with both prisms and fibers.

2-8, where the white line along the length of the dendrite (longitudinally across one of the fibers) shows the surface roughness. Surface roughness was calculated using the filter kernel for a Gaussian filter, where the average roughness (R_a) and root-mean-square roughness (R_q) were calculated by:

$$R_a = \frac{1}{n_x n_y} \sum_{i=1}^{n_x} \sum_{j=1}^{n_y} |Z_{(i,j)} - Z_{ave}| \quad (2.1)$$

$$R_q = \sqrt{\frac{\sum_{i=1}^{n_x} \sum_{j=1}^{n_y} [Z_{(i,j)} - Z_{ave}]^2}{n_x n_y}} \quad (2.2)$$

where $Z_{(i,j)}$ represents surface topography, Z_{ave} is the average surface roughness and the i, j values denote the pixels in directions x and y . The maximum default pixel values for the software were $n_x = n_y = 256$.

Interestingly, the observations for alternating Raman intensities corresponded to the height and roughness of the structures analyzed. The prismatic structures provided stronger Raman intensities than the fiber structures. The average roughness for the fibers was 16.6 nm in the longitudinal direction. A transversal line was also traced along the surface of the

crystal structures. The positions of the fibers are evident from the height profiles shown in Figure 2–8, where the average surface roughness was 33.8 nm.

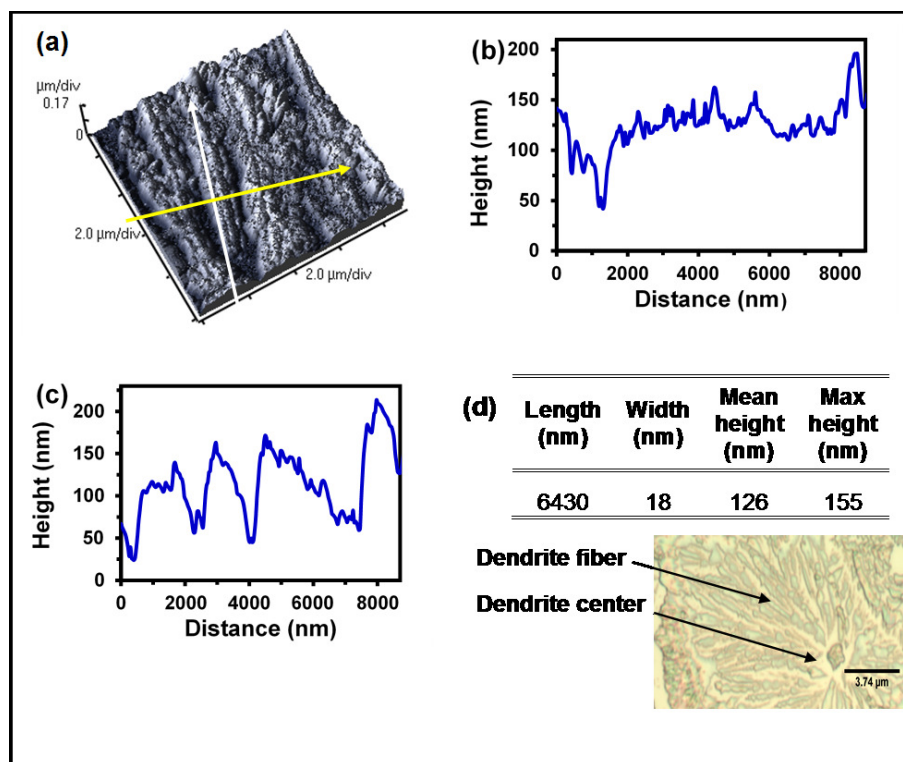


Figure 2–8: AFM imaging and analysis of the RDX dendrite fibers produced at 3k rpm: (a) topographical imaging; (b) height profile of longitudinal line (white); (c) height profile of the fibers along the transversal line (yellow); and (d) fiber dimensions determined from (b) and (c).

One possible explanation for the presence of polymorphs after the spin coating process at a given f value may be the mechanical influence of nucleation during the coating process. This has been discussed in detail for the pharmaceutical applications of crystal growth and polymorphism induced by pressure and temperature.^{24,25} In addition, solvent choice and stress by mechanical conversion are also known to induce polymorphism.^{1,2,11,24} Recent studies have classified the crystalline structure of α -RDX as orthorhombic.³⁵ However, this study established that the β -polymorph predominantly forms on the smooth SS surface at low f values as well as specific solubility parameters at room temperature and ambient pressure using an optimized spin coating methodology. With the information gathered from

Table 2–1: Spectral tests for the coexistence of α/β -RDX polymorphs with increase in f value.

| Rotational Speed (f ,rpm) | α -RDX | β -RDX | τ_f/τ_{3k} |
|---------------------------------|---------------|--------------|--------------------|
| 3k | 6.6 | 93.4 | 1.0 |
| 4k | 12.06 | 87.94 | 1.5 |
| 5k | 33.05 | 66.95 | 2.2 |
| 6k | 44.6 | 55.4 | 2.8 |
| 7k | 39.3 | 60.7 | 3.6 |
| 8k | 34.56 | 65.44 | 4.4 |

the scores for PCA using FT-IR, the percentage of α -RDX and β -RDX was calculated using the following equation:

$$\% \alpha\text{-RDX} = \frac{nk - b}{a - b} \times 100 \quad (2.3)$$

where the term nk represents the score value for the spectra selected for evaluation at each f value, a represents the average of the scores for α -RDX spectra, and b the average of the scores for β -RDX spectra.³⁴ The results are listed in Table 2–1, where shear stress (τ) is expressed as a ratio with respect to the f value of 3k rpm. A clear tendency to increase the percentage of α -RDX polymorph present on the substrate as f increased was found. This trend may be influenced by the solvent choice (acetone). There is evidence of coexistence and rate of crystallization in drop casting techniques due to solvent-mediation.^{1,7,8,20}

2.4.5 Solvent-Mediated Transformation to α -RDX

Additional studies by Raman microspectroscopy showed the possible presence of solvent traces after the spin-coating deposition process. Even after changing the drying protocol from using dry air to using high purity nitrogen gas, the presence of the vibrational modes for acetone were noticed at 787 cm^{-1} in Figure 2–9. Spectroscopic evidence to demonstrate the presence of traces of IPA was also evaluated, however the vibrational spectra analyzed showed no evidence of the presence of IPA. The spectra were collected as vibrational map measurements (Renishaw InVia, Raman 532 nm excitation) in an area where voids and

crystals of RDX were present after spin coating at 3k rpm. These measurements provided evidence of Stranski-Krastanov growth and evidenced a solvent-mediated transition to form α -RDX due to the presence of three peaks at the $-\text{CH}$ stretch region at 2952, 3006 and 3080 cm^{-1} (not shown in Figure 2–9).

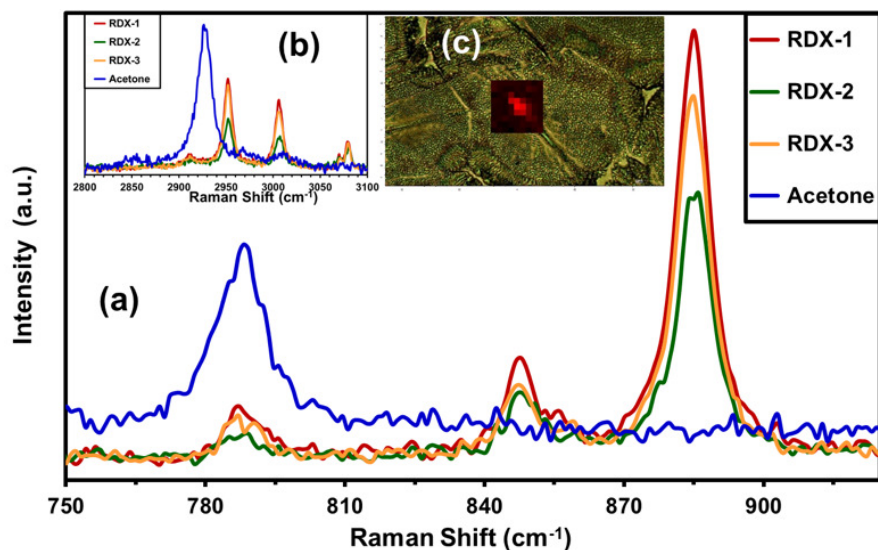


Figure 2–9: Vibrational Raman modes of solvents and RDX: (a) fingerprint region; (b) $-\text{CH}$ region; (c) micrograph and chemical image of Raman intensities at 887 cm^{-1} .

2.5 CONCLUSIONS

While the literature for the past half century has described α - and β -RDX as having different crystal structures, our results agree with recent studies where RDX polymorphs exhibit morphological variations within substrates. Therefore, one cannot rely solely on crystalline structures to distinguish between α/β -RDX polymorphs. To distinguish clearly between the two main forms of RDX at room temperature and atmospheric pressure, spectroscopic data were necessary to elucidate the conformers giving way to the various crystalline formations (dendrites, islands, and prisms). With this spectroscopic information, polymorphic features were visualized using PCA. For the RAIRS spectra of RDX deposits from concentrated solutions, a tendency of coexistence was observed with increasing f values and a high presence of the β -RDX polymorph. This coexistence was not as obvious for the FT-IR measurements, yet found in smaller regions for Raman measurements. Deposits

formed from less concentrated RDX solutions led to FT-IR reference β -RDX spectra. These spectra were correlated to the spectra taken for low f values from concentrated solutions, where the β -RDX form dominated the crystalline surface deposits. In morphological studies, a marked arrangement of dendrite structures was unveiled for the microscopic images of 3k and 8k rpm, for which the Raman spectra were consistent with the reported α -RDX polymorph. Various spots near the center and corners of each substrate were investigated with Raman micro spectroscopy to determine coexistence or presence of these polymorphs. Two of the SS substrates (prepared at 7k and 8k rpm) upon close inspection of the FT-IR and Raman spectra, as well as with discrimination by PC1, contained both polymorphs. This was clearly seen in the PCA scores plot for infrared spectra shown in Figure 2-3. RDX polymorphs coexistence was also confirmed by Raman spectra. RAIRS spectra were averaged for the CH region. The low intensity peak of the equatorial $-\text{NO}_2$ group appeared in the 7k rpm spectrum. This was due to the presence of the acetone solvent, which could remain trapped due to the immediate evaporation of the surface RDX. While the surface distribution seemed to remain homogeneous right after the spin coating process, detailed examination showed small regions of variation of deposited material within the substrates. Intensity variations in the Raman spectra of the crystals in this region confirmed the coexistence of RDX polymorphs at 7k rpm. FT-IR vibrational signatures and assignments were well correlated with the reported values in literature for the α - and β -RDX polymorphs. Further evidence of Stranski-Krastanov formation were evidenced by the presence of solvent in the contiguous areas to α -RDX crystals. This supports the hypothesis of solvent-mediated conversion from β -RDX to α -RDX. No presence of solvent was found in Raman mapping measurements at 632 nm for β -RDX. The characterization of these structures by AFM and white light microscopy provided evidence of a drastic change in morphology as f increased. Dendritic structures were noticed at 3k, 4k, and 5k rpm, while prismatic structures were

present at higher f values. The full characterization of these spectral features should provide information for preparation of test samples and standards and for generating spectral libraries for defense, security, and forensic applications.

REFERENCE LIST

- [1] I.G. Goldberg and J.A. Swift. New insights into the metastable β form of rdx. *J. Cryst. Growth Des.*, 12:1040–1045, 2012.
- [2] D.I. Millar, I.D. Oswald, D.J. Francis, W.G. Marshall, C.R. Pulham, and A.S. Cumming. The crystal structure of β -rdx an elusive form of an explosive revealed. *Chem. Commun.*, 5:562–564, 2009.
- [3] S. Hunter, T. Sutinen, S.F. Parker, C.A. Morrison, D.M. Williamson, S. Thompson, P.J. Gould, and C.R. Pulham. Experimental and dft-d studies of the molecular organic energetic material rdx. *J. Phys. Chem. C.*, 117:8062–8071, 2013.
- [4] Z.A. Dreger and Y.M. Gupta. High pressure raman spectroscopy of single crystals of hexahydro-1,3,5-trinitro-1,3,5-triazine (rdx). *J. Phys. Chem. B.*, 111:3893–3903, 2007.
- [5] F.P. Fabbiani and C.R. Pulham. High-pressure studies of pharmaceutical compounds and energetic materials. *Chem. Soc. Rev.*, 35(10):932–942, 2006.
- [6] T. Threlfall. Structural and thermodynamic explanations of ostwald’s rule. *Org. Process Res. Dev.*, 7:1017–1027, 2003.
- [7] I.G. Goldberg. *Directed crystal growth and solid-state analysis of the secondary explosives RDX and HMX*. PhD thesis, Georgetown University, Ann Arbor, MI, 2011.
- [8] Y. Diao, B.C.K. Tee, G. Giri, J. Xu, D.H. Kim, H.A. Becerril, R. M. Stoltenberg, T.H. Lee, G. Xue, S.C.B. Mannsfeld, and Z. Bao. Solution coating of large-area organic semiconductor thin films with aligned single-crystalline domains. *Nat. Mater.*, 12:665–671, 2013.
- [9] P. Torres, L. Mercado, I. Cotte, S.P. Hernández, N. Mina, A. Santana, R.T. Chamberlain, R. Lareau, and M.E. Castro. Vibrational spectroscopy study of beta and alpha rdx deposits. *J. Phys. Chem. B.*, 108:8799–8805, 2004.

- [10] R. Infante-Castillo, L.C. Pacheco-Londoño, and S.P. Hernández-Rivera. Monitoring the $\alpha \rightarrow \beta$ solidsolid phase transition of rdx with raman spectroscopy: A theoretical and experimental study. *J. Mol. Struct.*, 970(1):51–58, .
- [11] I.R. Lewis, N.W. Jr. Daniel, and P.R. Griffiths. Interpretation of raman spectra of nitro-containing explosive materials. part i: Group frequency and structural class membership. *Appl. Spectrosc.*, 51(12):1854–1867, 1997.
- [12] P. J. Miller, S. Block, and G. Piermarini. Effects of pressure on the thermal decomposition kinetics, chemical reactivity and phase behavior of rdx. *J. Combust. Flame.*, 83:174–184, 1991.
- [13] D.I. Millar, H.E. Maynard-Casely, A.K. Kleppe, W.G. Marshall, C.R. Pulham, and A.S. Cumming. Putting the squeeze on energetic materials-structural characterisation of a high-pressure phase of cl-20. *Cryst. Eng. Comm.*, 12:2524–2527, 2010.
- [14] D.I. Millar, W.G. Marshall, I.D. Oswald, and C. R. Pulham. High-pressure structural studies of energetic materials. *Crystallogr. Rev.*, 16:115–132, 2010.
- [15] W. McCrone. Crystallographic data. 32. rdx (cyclotrimethylenetrinitramine). *Anal. Chem.*, 22(7):954–955, 1950.
- [16] R.J. Karpowicz and T.B. Brill. Comparison of the molecular structure of hexahydro-1, 3, 5-trinitro-s-triazine in the vapor, solution, and solid phases. *J. Phys. Chem.*, 88(3):348–352, 1984.
- [17] R.J. Karpowicz, S.T. Sergio, and T.B. Brill. β -polymorph of hexahydro-1, 3, 5-trinitro-s-triazine. a fourier transform infrared spectroscopy study of an energetic material. *Ind. Eng. Chem. Prod. Res. Dev.*, 22(2):363–365, 1983.
- [18] J.A. Ciezak, T.A. Jenkins, and Z. Liu. Evidence for a highpressure phase transition of ϵ 2, 4, 6, 8, 10, 12hexanitrohexaazaisowurtzitane (cl20) using vibrational spectroscopy. *Propellants Explos. Pyrotech.*, 32:472–477, 2007.
- [19] R. Hultgren. An xray study of symmetrical trinitrotoluene and cyclo trimethylenetrinitramine. *J. Chem. Phys.*, 4:84, 1936.

- [20] *Fundamentals of Nucleation Theory. In Nucleation Theory and Growth of Nanostructures.* Springer Berlin Heidelberg, 2014. ISBN: 978-3-642-39659-5.
- [21] A. Lorke, R. Blossey, J. M. Garcia, M. Bichler, and G. Abstreiter. Morphological transformation of inorganic islands, fabricated by stranski-krastanov growth. *Mater. Sci. Eng. B.*, 88:225–229, 2002.
- [22] B. Wedl, R. Resel, G. Leising, B. Kunert, I. Salzmann, M. Oehzelt, N. Koch, A. Vollmer, S. Duhm, O. Werzer, G. Gbabode, M. Sferrazza, and Y. Geerts. Crystallisation kinetics in thin films of dihexyl-terthiophene: the appearance of polymorphic phases. *RSC Adv.*, 2:4404–4414, 2012.
- [23] G. Capellini, L. Di Gaspare, F. Evangelisti, and E. Palange. Atomic force microscopy study of self-organized ge islands grown on si(100) by low pressure chemical vapor deposition. *Appl. Phys. Lett.*, 70:493–495, 1997.
- [24] S.Y. Lin, W.T. Cheng, and S.L. Wang. Thermal micro-raman spectroscopic study of polymorphic transformation of famotidine under different compression pressures. *J. Raman Spectrosc.*, 38:39–43, 2007.
- [25] S.Y. Lin and W.T. Cheng. The use of hot-stage microscopy and thermal micro-raman spectroscopy in the study of phase transformation of metoclopramide hcl monohydrate. *J. Raman Spectrosc.*, 43(8):1166–1170, 2012.
- [26] W.T. Cheng, S.Y. Lin, and M.J. Li. Raman microspectroscopic mapping or thermal system used to investigate milling-induced solid-state conversion of famotidine polymorphs. *J. Raman Spectrosc.*, 2017.
- [27] W. Bachmann and J.C. Sheehan. A new method of preparing the high explosive rdx. *J. Am. Chem. Soc.*, 71:1842–1845, 1949.
- [28] W.M. Hikal, J.T. Paden, and B.L. Weeks. Thermo-optical determination of vapor pressures of tnt and rdx nanofilms. *Talanta*, 87:290–294, 2011.

- [29] E.D. Emmons, M.E. Farrell, E.L. Holthoff, A. Tripathi, N. Green, R.P. Moon, J.A. Guicheteau, S.D. Christesen, P.M. Pellegrino, and A.W. Iii, Fountain. Characterization of polymorphic states in energetic samples of 1,3,5-trinitro-1,3,5-triazine (rdx) fabricated using drop-on-demand inkjet technology. *Appl. Spectrosc.*, 66:628–635, 2012.
- [30] M. Wrable-Rose, O.M. Primera-Pedrozo, L.C. Pacheco-Londoño, and S.P. Hernández-Rivera. Preparation of tnt, rdx and ammonium nitrate standards on gold-on-silicon surfaces by thermal inkjet technology. *Sens. Imaging.*, 11(4):147–169, 2010.
- [31] *Applications of Fiber Optic Coupled-Grazing Angle Probe Reflection-Absorption FTIR Spectroscopy, in Fourier Transforms - New Analytical Approaches and FTIR Strategies.* INTECH Open Access, Croatia, 2011. ISBN 978-953-307-232-6.
- [32] R.G. Greenler. Infrared study of absorbed molecules on metal surfaces by reflection techniques. *J. Chem. Phys.*, 44:310–314, 1996.
- [33] R. Infante-Castillo, L.C. Pacheco-Londoño, and S.P. Hernández-Rivera. Vibrational spectra and structure of rdx and its 13c- and 15n-labeled derivatives: A theoretical and experimental study. *Spectrochim. Acta, Part A.*, 76(2):137–141, 2010.
- [34] C.S. Garcia, M.N. Abedin, S.K. Sharma, A.K. Misra, S. Ismail, U.N. Singh, T.F. Refaat, S.P. Sandford, and H.E. Elsayed-Ali. Design and build a compact raman sensor for identification of chemical composition. *Proc. SPIE.*, 6943:69430i/1–69430i/7, 2006.
- [35] H.M. Shim and K.K. Koo. Crystal morphology prediction of hexahydro-1,3,5-trinitro-1,3,5-triazine by the spiral growth model. *Cryst. Growth Des.*, 14:1802–1810, 2014.

CHAPTER 3

OPTICAL PROPERTIES OF β -RDX THIN FILMS DEPOSITED ON GOLD AND STAINLESS STEEL SUBSTRATES CALCULATED FROM REFLECTION-ABSORPTION INFRARED SPECTRA

Published in: *Journal of Applied Spectroscopy*. José L. Ruiz-Caballero, Joaquín A. Aparicio-Bolaño, Amanda M. Figueroa-Navedo, Leonardo C. Pacheco-Londoño, and Samuel P. Hernández-Rivera. DOI: [10.1177/0003702817710248](https://doi.org/10.1177/0003702817710248)

3.1 LITERATURE REVIEW

Interest in the study and characterization of α/β -RDX polymorphism has increased based on recent reports.¹⁻⁸ These investigations describe the crystallization phenomena under various deposition environments such as spin coating technology,¹ drop-on-demand inkjet technology,² changes in both temperature and pressure,³⁻⁶ and liquid inclusion phenomenon.⁷ As is well known, in the solid state phase, the highly energetic material (HEM) cyclic nitramine hexahydro-1,3,5-trinitro-s-triazine (RDX)⁹ preferentially conforms to the chair configuration of a six-membered ring (s-triazine or 1,3,5-triazine ring). The polymorphism exhibited by RDX is associated with the relative position of the three nitro (NO₂) groups in either equatorial or axial positions with respect to the s-triazine ring.¹⁰ The α -RDX polymorph has been long established as the stable form at room temperature.¹¹ The orientations of the NO₂ groups in this case are two axial and one equatorial orientations, rendering a C_s symmetry to the conformation (axial-axial- equatorial RDX or AAE-RDX). The conversion from α -RDX to γ -RDX is theoretically demonstrated when the nitro groups

change from AAE-RDX to EEA-RDX, preserving the same symmetry.¹² The molecular conformation referred to as β -RDX has the NO_2 groups occupying all axial orientations with respect to the s-triazine ring (axial-axial-axial RDX or AAA-RDX) and a symmetry corresponding to C_{3v} .¹³⁻¹⁵ There have been many reports in the scientific literature regarding RDX since its discovery in 1889 (by G. Henning, German Patent No. 104280). Initially, the use of RDX was based on its potential pharmacological properties. Presently, this compound is considered an essential ingredient for military shells, bombs, landmines, grenades, demolitions operations, and underwater blasting.¹⁶ As part of the detection protocol, sensors require standards that can serve as target compounds such as HEMs with well-characterized properties to be validated. Since the discovery of RDX, numerous researchers have studied its physical and chemical properties,¹⁷ but the RDX polymorphism of crystalline films prepared by deposition on substrates that can be used as samples and standards has received little attention.^{2,18-21} Recently, we reported on the parameters of a spin-coating deposition methodology required to generate RDX crystalline films whose polymorphic distribution was favored by β -RDX.¹ Raman chemical images were carried out across a region of $40 \times 40 \mu\text{m}$ (81 spectra) for SS substrates that were kept for over 2 years. Crystals of β -RDX were still present on the SS substrates. Goldberg and Swift were the first to confirm the stability of β -RDX.⁸ Contributions along this line of effort by Wrable and co-workers¹⁸ determined the residence time of RDX on various substrates. However, the optical properties (OP) have not been reported before using reflection-absorption infrared spectroscopy (RAIRS). Isbell and Brewster²² obtained RDX optical constants using infrared (IR) transmission spectra.

Fourier transform IR (FT-IR) spectroscopy has vast applications in this area and provides the requirements necessary to characterize both ultrathin films (UTFs) and substrates. FT-IR spectroscopy has two (2) important properties that offer practical advantages for the optical properties characterization of thin films. First, it is one of a few techniques that can be used for *in situ* studies of chemical, physical, and biological processes on surfaces and at sample interfaces.²³⁻²⁵ Second, it is highly useful in monitoring UTFs of absorbates for

applications in fields such as optoelectronics and microelectronics of inorganic materials.²³ A UTF may be on the order of 100 nm (or slightly more). FT-IR spectroscopy has the sensitivity to analyze these films and even smaller thickness films. These films are usually known as monolayers. Finally, if FT-IR micro spectroscopy itself does not provide the sensitivity to analyze thinner films, then a good alternative is to use reflection-absorption infrared spectroscopy coupled to FT-IR (FT-IR/RAIRS).²⁶

An in-depth knowledge of the optical properties of materials enables the development of devices for various applications in nanocircuits, molecular sensors, etc.²⁴ Optical properties also have great significance in energetic material research such as laser pyrolysis, laser-assisted combustion and ignition.²⁵ In the IR spectral region, optical properties are commonly obtained using two different approaches: measurements of transmission spectra, which are also used to identify the chemical structure by correlating the absorption peaks with the individual bonds and lattice vibrations, and measurements of reflection-absorption spectra. The latter is a very sensitive optical technique for measuring low concentrations of an absorbent material adhered to reflective surfaces.^{27,28} It is possible to obtain the optical properties of the material under investigation from information contained in the reflection-absorption spectra of a material adhered to a given substrate. In addition, important aspects derived from material conductivity, such as the correlation between the electrical properties of the material and a specific optical property, are critical for sensor development applications.^{29,30}

To determine the optical constants using FT-IR/RAIRS, it is essential to previously obtain the following information on the experimental conditions: film thickness, relative intensity of IR absorption bands, angle of incidence of the electromagnetic radiation, and electric field vector polarization state.³¹ This last attribute is associated with the experiment setup and addresses the polarization of light and reflective mode in the experiments. The veracity of these suggestions is supported by the comparison of the findings of this study with those by other authors.³² Several authors have formulated several equations in which

these optical constants are calculated from the boundary condition problem derived from Maxwell equations.^{27,28,33} After the exact model for an adsorbate on a (highly reflective) metal substrate is identified, the correct equations must be selected to solve the problem on hand.

Several techniques can be used to measure the sample film thickness,^{34,35} for example, (a) *in vacuum*: X-ray photoelectron spectroscopy (XPS), Auger electron spectroscopy (AES), and ion-based methods such as low-energy ion scattering (LEIS) and secondary-ion mass spectrometry (SIMS); (b) ellipsometry via modeling of the optical constants; (c) the quartz crystal microbalance (QCM) method; and (d) atomic force microscopy (AFM). In the present work, AFM operated in the non-contact mode is the technique used to measure the sample thicknesses.

3.2 EXPERIMENTAL

3.2.1 Reagents

Acetone (CH_3COCH_3 , HPLC+, 99.9%), methanol (CH_3OH , 99.9% HPLC grade), isopropyl alcohol ($\text{CH}_3\text{CH}(\text{OH})\text{CH}_3$, 99.7%), and acetonitrile (CH_3CN , HPLC+, 99.9%) were acquired from Sigma-Aldrich Chemical Co., (Milwaukee, WI, USA). Standard solutions of RDX: 1000 ppm in acetonitrile and GC/MS primary standard grade were obtained from Restek Corp. (Bellefonte, PA, USA) and Chem Service, Inc., (West Chester, PA, USA), respectively. RDX was synthesized according to the Bachmann method with slight modifications.³⁶ Solvents and materials for RDX synthesis: hexamethylenetetramine ($((\text{CH}_2)_6\text{N}_4$, 99% w/w) was purchased from Sigma-Aldrich Chemical Co. Sodium nitrite (NaNO_2 , 99%) was purchased from Acros Organics (Morris Plains, NJ, USA). Fuming nitric acid (HNO_3 , 97% w/w) and nitric acid (HNO_3 , 70%, w/w) were purchased from Fisher Scientific International (Chicago, IL, USA). The water used to prepare the solutions and clean and rinse glassware was deionized and doubly distilled (18 M Ω /cm) to make it HPLC grade. Stainless steel (SS) substrates ($1.0 \times 1.0 \text{ in}^2$) were purchased from Stainless Supply, Inc. (Monroe,

NC, USA). Gold-coated standard microscope slides, which were used as substrates (75×25 mm², 1 mm thickness), were acquired from Ted Pella, Inc. (Redding, CA, USA).

3.2.2 Instrumentation and Experimental Setup

A spin-coating system (model 6800, Specialty Coatings Systems, Inc., Indianapolis, IN, USA) was used for the RDX sample deposition. The optical constants for both substrates were measured at 3000 revolutions per minutes (3k rpm). The ramp-up time was 2 s with a dwell time of 5 s, and the ramp-down time was 5 s with a dwell time of 0 s. Five (5) s was a reasonable time to decrease the rotation frequency because it was sufficient to ensure higher sample hold down and avoid breaking the adhesion/cohesion surface forces of the film, thus preventing loss of uniformity by inertia. The spin coater interior was purged with highly filtered dry air. This was the same methodology as that reported previously to ensure reproducibility.¹

A Bruker Optics IFS-66 v/s evacuable FT-IR interferometer (Bruker Optics, Billerica, MA, USA) was used for the mid-infrared MIR measurements. This system was equipped with a DGTS detector and accessories to measure the reflection and polarization of light. The IR spectral data in this work were analyzed using the OpusTM software suite (v. 6.0, Bruker Optics). A variable angle reflection accessory model A 513/Q (Bruker Optics) was used for the measurements. All reflectance data were collected at 80° of incidence, which is reported as the most convenient and reproducible value for grazing angle measurements.^{1,26,37,38} The MIR polarizer was a model M 21-07/08 (Bruker Optics). The rotatable holder permitted an angular position at two angles of polarization with respect to the plane of incidence: perpendicular (s-polarized) and parallel (p-polarized). These polarization states of light are essential to characterize the optical properties in a reflective medium because they favor specific vibration modes. The area of the analyzed samples was 1.0×1.0 in². The FT-IR interferograms were collected in the 500–1800 cm⁻¹ spectral range with a 4 cm⁻¹ nominal spectral resolution, 1000 scans as background per sample scan, and a scanner velocity set at 4.0 kHz.

High-pressure liquid chromatography (HPLC) runs were performed in an Agilent 1100 series equipped with a C-18 column model Eclipse XDB platinum, 100 Å, 5 μm , 150 mm by 4.6 mm (Grace-Alltech, Grace Discovery Sciences, Columbia, MD, USA), and a variable wavelength detector, which was set to 254 nm. Borosilicate glass scintillation vials (Fisher Brand, Thermo-Fisher Scientific) sealed with TeflonTM screw caps and ultrasonic equipment were used to prepare the solutions. The solution preparation conditions were as follows: (a) 6 μL injection, (b) 0.7 mL flow rate, (c) 50% methanol/water, (d) column temperature of 27°C, and (e) detector wavelength of 254 nm. These setup conditions enabled us to estimate the RDX standard solution purity from its synthesis.

An AFM (model Ntegra Spectra; NT-MDT America, Inc., Tempe, AZ, USA) was used to characterize the topography, morphology, and thickness of the prepared coatings. The cantilever in the non-contact mode had a frequency of 340.95 kHz. Image AnalysisTM software v.3.5.0.16646 (NT-MDT SPM Software), provided with the equipment, was used to evaluate the captured AFM images.

3.2.3 Preparation of Au Substrates

The RDX crystals (99.9%) were separately dissolved in two solvents: isopropyl alcohol to saturation (2.21×10^{-4} M) and acetone (2.00×10^{-1} M), as described in previous works.^{1,17} Subsequently, the substrates were cleaned and sonicated using acetone; then, they were rinsed with distilled water and isopropyl alcohol. To ensure that no residual solvent persisted after washing, the Raman spectra were collected. In the experiment, first, an aliquot of each solution (30 μL) was transferred to the substrate for approximately 2 s; then, the spin coating routine was performed as previously described. The Au substrates had an area of 1.0×1.0 in².

3.3 RESULTS AND DISCUSSION

3.3.1 AFM Characterization and Determination of the Surface Concentration

Thin film deposition by spin coating offers considerable advantages compared with methods such as: sample smearing²⁶ drop casting,³⁹ air spraying,⁴⁰ pneumatically assisted

nebulization,⁴¹ etc. It because is less subject to human error and provides a reliable coated surface for optical property studies.⁴² An effective coating depends on both the operational parameters and the chemical properties of the adsorbate and substrate. The RDX crystalline films on SS substrates prepared with rapid spinning rates exhibit an increase in the ratio of α -RDX polymorph to β -RDX polymorph.¹ In fact, spin-coating deposition at 3000 rpm changes the α/β distribution and favors crystalline films of the less stable β -RDX.¹ The AFM measurements show that the mean height of the β -RDX crystalline films on SS substrates was 126 nm. A similar procedure at 3k rpm generated β -RDX crystalline films deposited on the Au substrates. The morphological studies were accompanied by characterization with polarized RAIRS studies. The topography data for the β -RDX crystalline films on gold substrates deposited at 3k rpm are shown in Figure 3-1. This illustration shows fiber-like structures in the form of dendrites, as previously discussed for SS substrates.¹ This result was also confirmed by Raman spectroscopy measurements. From these results, the mean height was found to be 175 nm. The surface roughness was calculated using the reported equations for SS substrates.¹ The purpose of this characterization is to estimate the film thickness (d , cm) in terms of the mean height for RDX crystalline films deposited on gold. These values are considered required input information for Equations 1.12 and 1.13.

An important finding is shown in Figure 3-2, where the unpolarized spectra of β -RDX crystalline films on Au substrate (β -RDX/Au) and SS substrate (β -RDX/SS) are compared. The most intense peak at $\sim 1588\text{ cm}^{-1}$, which is tentatively assigned to the asymmetric stretching of the nitro-axial group, was used for the calculations. The peak intensity of β -RDX/Au (from Figure 3-2(a), blue trace) was 1.5-fold the intensity of β -RDX/SS (Figure 3-2(b), red trace). This result corroborates that the thickness of β -RDX/Au was 1.4-fold that of β -RDX/SS. In other words, the peak intensity ratios prove the importance of using IR spectroscopy to obtain the optical properties. In addition, RAIRS can be used to

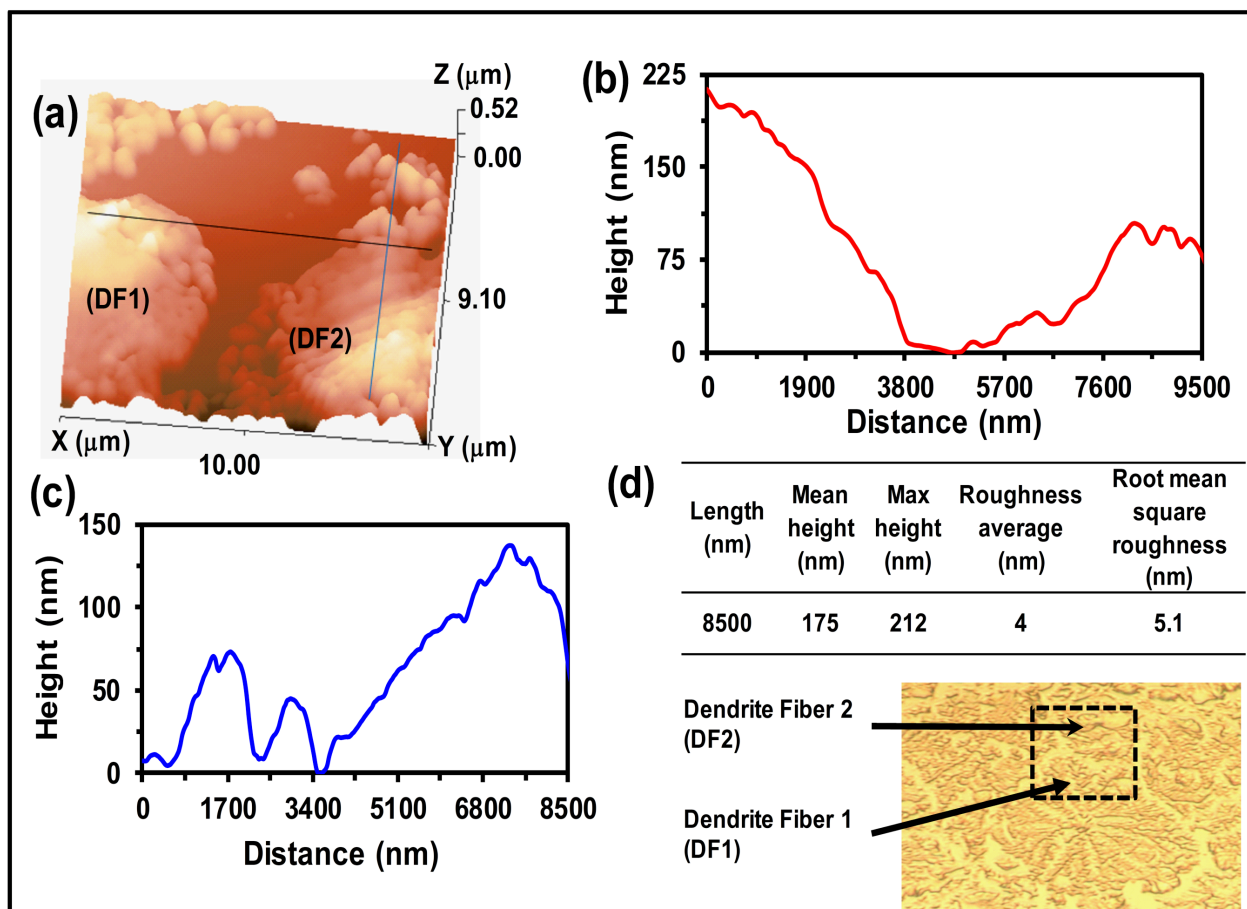


Figure 3–1: AFM image and analysis of predominantly β -RDX dendrite fibers (DF1 and DF2) formed at 3k rpm on Au substrates: (a) topographical imaging; (b) height profile of the horizontal line (black); (c) height profile of the fibers (DF2) along the vertical line (blue); (d) fiber dimensions determined from (b) and (c).

study the distribution of different components in the matrices and surfaces throughout the sample.⁴¹

In another experiment, RDX was deposited on Au substrates using two solutions of markedly different concentrations. Samples were prepared using the described spin-coating deposition procedure. The concentrations of the solutions were as follows: 49 ppm RDX in isopropyl alcohol (or 2.20×10^{-4} M) and 2.00×10^{-1} M RDX in acetone. The unpolarized FT-RAIRS spectra for the samples after the spin-coating deposition of these solutions are shown in Figure 3–3. Raman spectroscopy was used to confirm the presence of β -polymorph in the RDX crystalline films on Au. The average thickness of the films based on the AFM

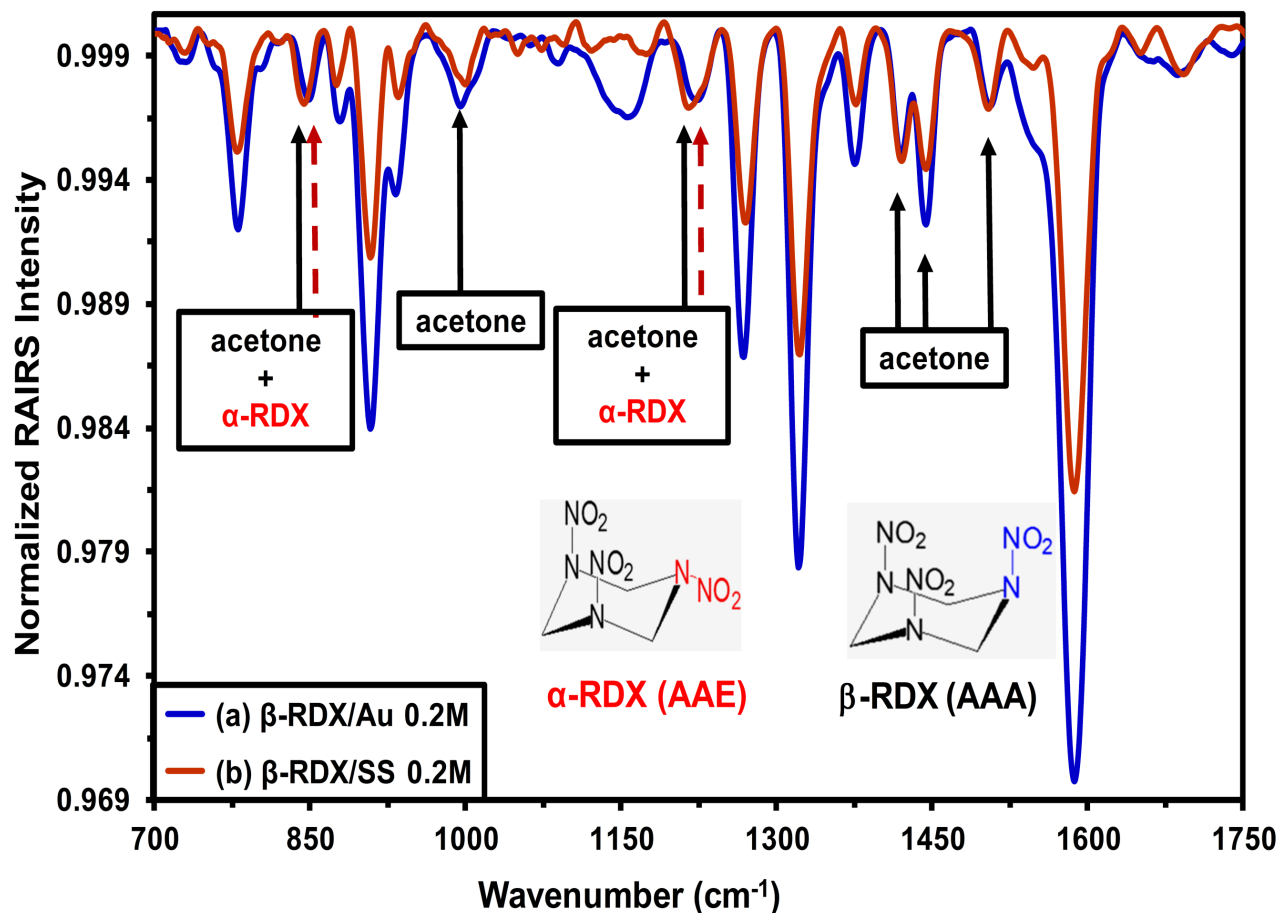


Figure 3–2: Unpolarized RAIRS spectra of predominantly β -RDX crystalline films on (a) Au substrates (blue trace) and (b) SS substrates (red trace). Solvent modes are presented with solid arrow, and the dashed arrows represent concomitant vibrational modes of the solvent and remaining α -RDX polymorph.

measurements was 78 nm. The average thickness of the β -RDX/Au crystalline films obtained from the deposition of the 2.00×10^{-1} M RDX solution (Figure 3–3(a), blue trace) was 2.24-fold larger than the corresponding thickness of β -RDX/Au crystalline films obtained from the deposition of the 2.20×10^{-4} M RDX solution (Figure 3–3(b), red trace). To further confirm this result, the same spectroscopic band (1588 cm^{-1}) was used to calculate the peak height intensity ratios. The peak height of β -RDX/Au crystalline films from 2.00×10^{-1} M was 2.27-fold that of β -RDX/Au crystalline films from 2.20×10^{-4} M. An important aspect of this contribution centered on estimating the thickness of β -RDX films upon sample deposition by spin coating on Au and SS substrates of the 2.00×10^{-1} M

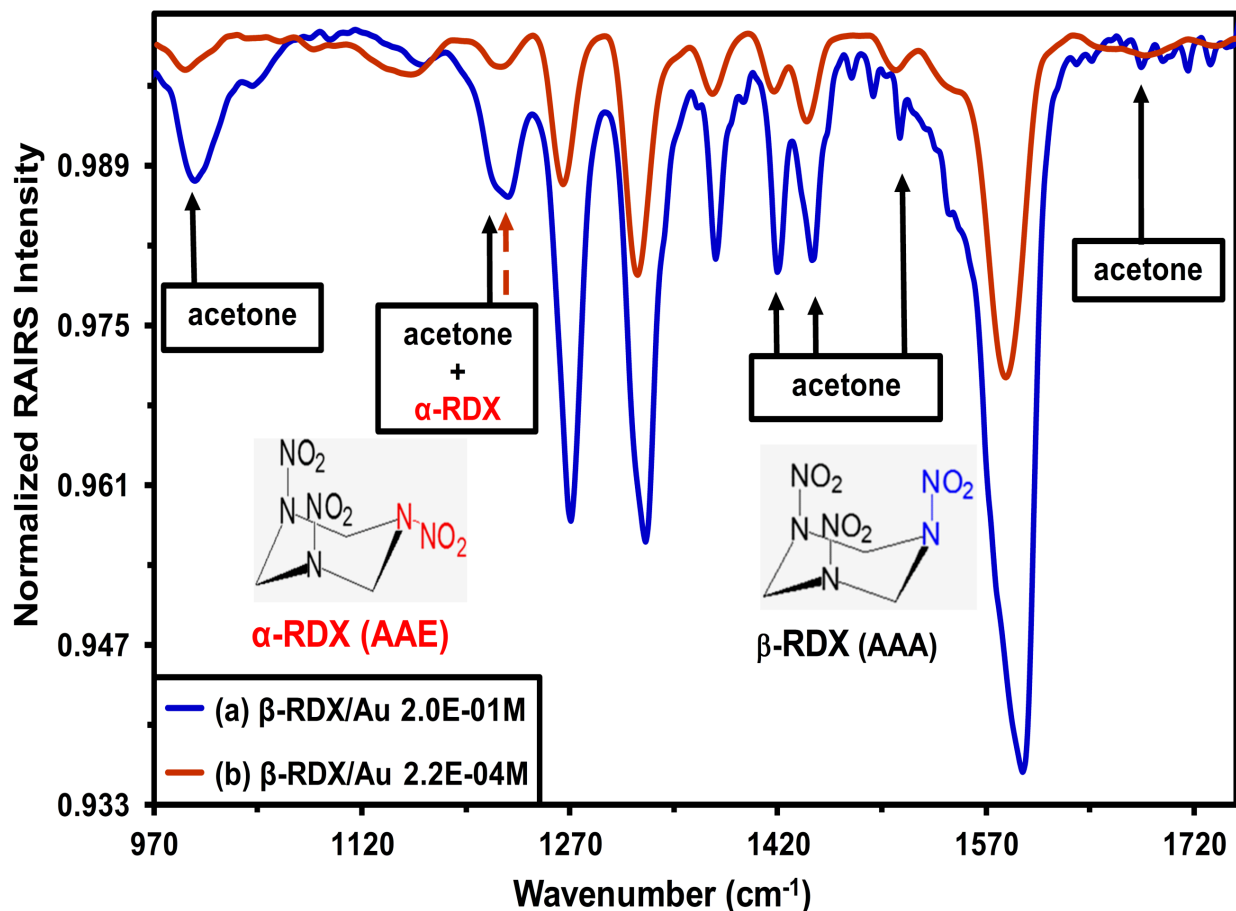


Figure 3–3: Unpolarized RAIRS spectra of predominantly β -RDX crystalline films on Au substrates at two concentrations: (a) 2.00×10^{-1} M (blue line) and (b) 2.20×10^{-4} M (red line). Solvent modes are presented with solid arrows and concomitant vibrational modes between solvent and remaining α -RDX polymorph are pointed with red dashed arrows.

solution of RDX in acetone. In this respect, many challenging factors had to be controlled, such as the fast nucleation rate, shear forces, centrifugal forces, viscosity, Coriolis force, gravitational gradient, and fluid density.

3.3.2 RAIRS Measurements

The parameters used to obtain both $\text{Im}(\hat{\varepsilon})$ and $\text{Im}(1/\hat{\varepsilon})$ have been defined as follows: the sample thickness d and angle of incidence φ_1 of the EMR (80° with respect to the surface normal vector). In the RAIRS experiments the spectral window of $1000\text{--}1800\text{ cm}^{-1}$ was used for the β -RDX crystalline films deposited on both substrates. This IR spectrum resulted from influences of both variables: the polarization state of the EMR field and incident

angle of the radiation. In fact, the imaginary parts of the permittivity, refractive index, and wave vector were activated by these parameters. The RAIRS spectrum of β -RDX/Au had higher intensity compared to β -RDX/SS, although both absorbates (β -RDX/Au and β -RDX/SS) were deposited under identical conditions of pressure, temperature, and spin-coating program. A plausible explanation for the reported intensity differences is the larger reflectivity of Au compared to SS.²⁷ These findings were corroborated by the AFM roughness measurements: the SS and Au substrates had average roughness values of 8 nm and 2 nm, respectively. Another important observation is related to the surface selection rules regarding the electric field vector: the observed IR signal intensities for p-polarized EMR were twice the s-polarized intensities.^{27-31,34,38,43-48} An inspection of the FT-RAIRS spectra for RDX clearly shows that this material is in the β -RDX conformation. The asymmetric stretching of the axial nitro group ($-\text{NO}_2$) was confirmed by the strongest band at 1587.2 cm^{-1} . Both asymmetric and symmetric in-plane bending of the $-\text{CH}_2-$ group from the s-triazine ring were evidenced by two peaks: one of higher intensity at 1444.5 cm^{-1} and the other at 1421.3 cm^{-1} .^{12,13} The peak at 1375 cm^{-1} was attributed to the out-of-plane bending of the $-\text{CH}_2-$ group from the s-triazine ring. The symmetric stretching of $-\text{N}-\text{NO}_2$ was located at 1321.0 cm^{-1} . The band at 1269.0 cm^{-1} was attributed to the $-\text{N}-\text{NO}_2$ stretching. Finally, the $-\text{N}-\text{C}-\text{N}$ stretching of the s-triazine ring was located at 1224.6 cm^{-1} . These assignments were consistently confirmed on both substrates. The assignments are consistent with the results of Infante et al.,¹¹ who reported experimental data and theoretical calculations on ^{13}C - and ^{15}N -RDX isotopomers and the α -RDX \longrightarrow β -RDX phase transition monitored by Raman spectroscopy.¹³ However, there are slight wavenumber shifts with respect to the values reported by Karpowicz et al.¹⁴ and Karpowicz and Brill¹⁴ for IR measurements of β -polymorph. These shifts can be attributed to the interactions with the surfaces on which the RDX was deposited. The interaction energies between absorbate

and substrate must be further studied to confirm these observations. As mentioned, β -RDX/Au and β -RDX/SS have different band intensities in the spectral range of 1420-1450 cm^{-1} because of the different optical properties in the MIR region.

3.3.3 Transversal and Longitudinal Optical Vibrations

The permittivity ($\hat{\varepsilon}$) is a macroscopic optical property of a medium, which is also very important at the atomic level and enables one to describe the interaction of the electric field of an incident EMR wave while propagating through the medium.^{45,46} The permittivity tensor characterizes the interactions of the electric field vector (\vec{E}) with the absorbent matter. According to the previously presented mathematical description, the imaginary part of permittivity, which is symbolized as $\text{Im}(\hat{\varepsilon}) = \varepsilon''$, is known as the longitudinal optical function. This function can be approximated using the relative intensity of the reflected MIR signal ($\frac{\Delta R}{R}$), sample thickness (d), EMR angle of incidence to the sample surface (φ_1), and IR wavenumber ($\tilde{\nu}$). The imaginary part of the permittivity can be calculated from Equation 1.13. The real part of the permittivity (ε') can be determined when the light is attenuated as:

$$\text{Re}(\hat{\varepsilon}) = \varepsilon' = \sqrt{\frac{\text{Im}(\hat{\varepsilon})}{\text{Im}\left(\frac{1}{\hat{\varepsilon}}\right)} - (\text{Im}(\hat{\varepsilon}))^2} \quad (3.1)$$

$\text{Im}\left(\frac{1}{\hat{\varepsilon}}\right)$ is the transversal optical function and can be determined from Equation 1.12. In addition, the peak maximum of the representation of the real part of the permittivity vs. the wavenumber corresponds to the transversal optical vibration ($\tilde{\nu}_{\text{TO}}$). The maximum representation of the imaginary part of the permittivity as a function of the wavenumber corresponds to the longitudinal optical vibration ($\tilde{\nu}_{\text{LO}}$). Figure 3-4 shows a plot of ε vs. $\tilde{\nu}$ for a β -RDX thin film deposited on a Au substrate. Representations of the real and imaginary components of the permittivity as functions of the wavenumber are included. The $\text{Re}(\hat{\varepsilon})$ and $\text{Im}(\hat{\varepsilon})$ peak maxima were at 1571.8 cm^{-1} and 1587.2 cm^{-1} , respectively. In this band, the asymmetric stretching of the axial nitro groups is activated as ($\tilde{\nu}_{\text{TO}}$)Au. This result is described by the peak maximum at 1587.2 cm^{-1} (Figure 3-4), which shows a high

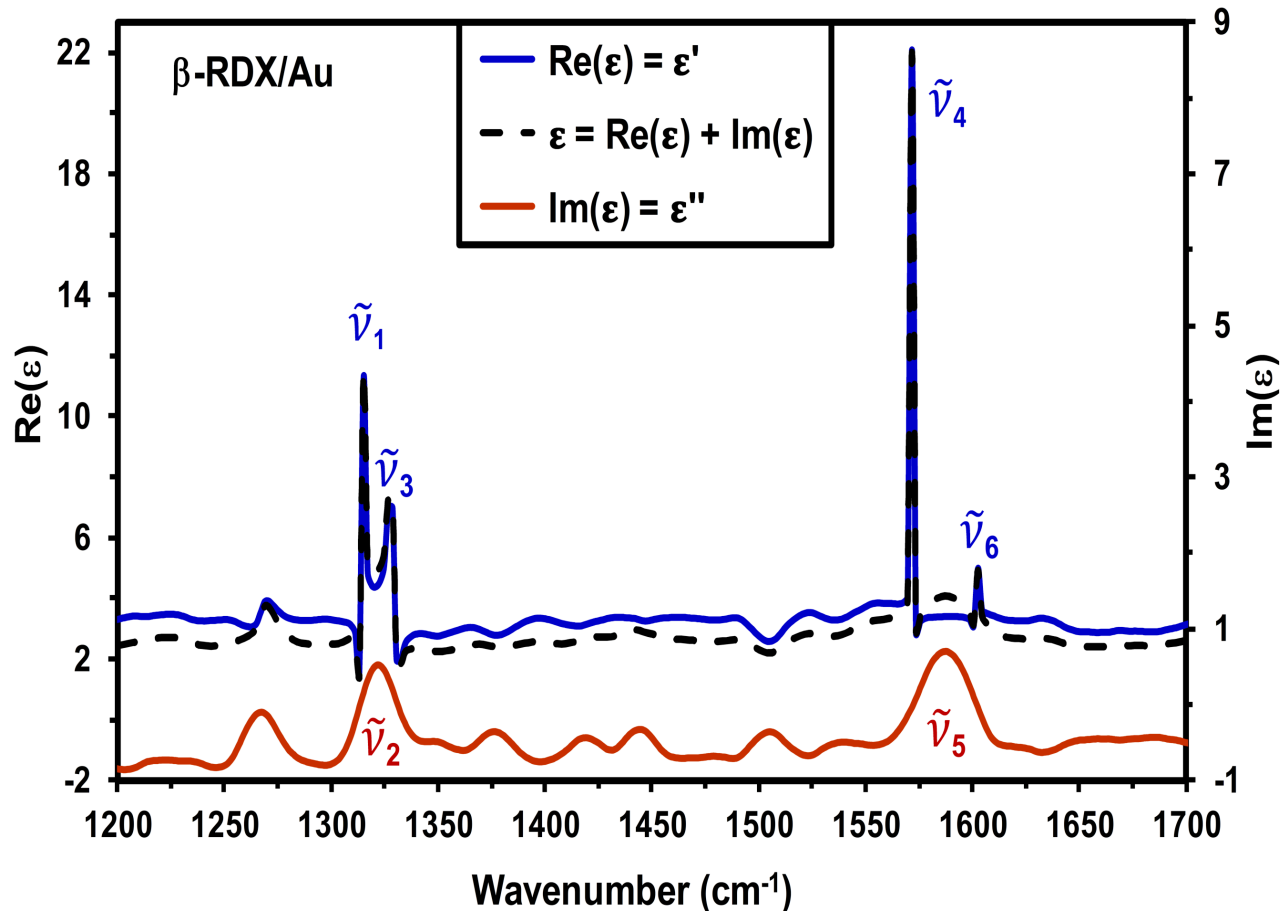


Figure 3-4: Permittivity (ε) of predominantly β -RDX crystalline films deposited on Au substrates (segmented black line). The transversal optical function is expressed as the imaginary part [$\text{Im}(\hat{\varepsilon})$; red trace] and real part [$\text{Re}(\hat{\varepsilon})$; blue trace] of the permittivity.

dynamic response of the asymmetric vibration mode of the axial nitro groups with respect to the external electric field vector.

In contrast, Figure 3-5 shows the β -RDX layers on SS substrates, where the peak maxima of $\text{Re}(\hat{\varepsilon})$ and $\text{Im}(\hat{\varepsilon})$ were 1315.3 cm^{-1} , and 1587.2 cm^{-1} , respectively. The results indicate two important aspects: (a) for both substrates, the transversal and longitudinal optical vibrations retain their peak maximum at 1587.2 cm^{-1} ; (b) the external electric field vector can mediate the activation of the vibration mode of the axial nitro groups as a function of the substrate through the β -RDX layers.

The obtained $\text{Re}(\hat{\varepsilon})$ and $\text{Im}(\hat{\varepsilon})$ from the RAIRS measurements of β -RDX crystalline films deposited on Au substrates ($(\text{Re}(\hat{\varepsilon}))\text{RDX}/\text{Au}$) suggest a high dynamic response, which

is evidenced by the asymmetric vibration mode of the axial nitro groups with respect to the incident external electric field vector. However, the $\text{Re}(\hat{\epsilon})$ and $\text{Im}(\hat{\epsilon})$ obtained from β -RDX crystalline films deposited on SS substrates ($(\text{Re}(\hat{\epsilon}))\text{RDX/SS}$) suggest that the $-\text{N}-\text{NO}_2$ symmetric stretch vibration modes are involved in this assembly. Nevertheless, it is difficult to assign the presented optical behavior to a surface phenomenon such as a specific molecular surface orientation because this assignment requires further corroboration with theoretical models and other experiments. The main objective of this study is to develop, optimize, and validate a procedure for producing samples of β -RDX crystalline films on Au and SS substrates and characterize the corresponding chemical and physical properties. Specifically, in this contribution, the β -RDX crystalline films deposited on Au and SS substrates were characterized by RAIRS.

3.3.4 Calculations of the Optical Constants for RDX/Au and RDX/SS

To characterize the interactions between RDX crystalline films (absorbing medium) and the incident electromagnetic wave, it is necessary to find information on (a) the permittivity $\hat{\epsilon}$, (b) refractive index \hat{n} , and (c) wave propagation vector \vec{k} . However, these macroscopic properties are not directly measurable. This work focuses on the behavior of optical constants when an absorbate (β -RDX crystalline film) is deposited on Au and SS substrates. The optical constants were graphed against the wavenumber $\tilde{\nu}$ of the incident EMR. Then, the resulting functions $n(\tilde{\nu})$, $k(\tilde{\nu})$, $\text{Im}[\varepsilon(\tilde{\nu})]$, and $\alpha(\tilde{\nu})$ were graphed against the reciprocal of lambda to generate the peak maxima. The Appendix B, contains Figures B-1 to B-5 in which these optical constants are shown as function of wavenumber ($\tilde{\nu}$).

Table 3-1 summarizes the information contained in Figures 3-6, where optical properties: $n(\tilde{\nu}) = \text{Re}[n(\tilde{\nu})]$, $k(\tilde{\nu}) = \text{Im}[n(\tilde{\nu})]$, and $\alpha(\tilde{\nu})$ were calculated. Two spectral windows in Figure 6: Region I ($1300 - 1350 \text{ cm}^{-1}$), highlighted in light green and Region II ($1550 - 1625 \text{ cm}^{-1}$), highlighted in light red. Table 3-1 shows six maximum values of the real and imaginary parts of n and k with respect to the substrates.

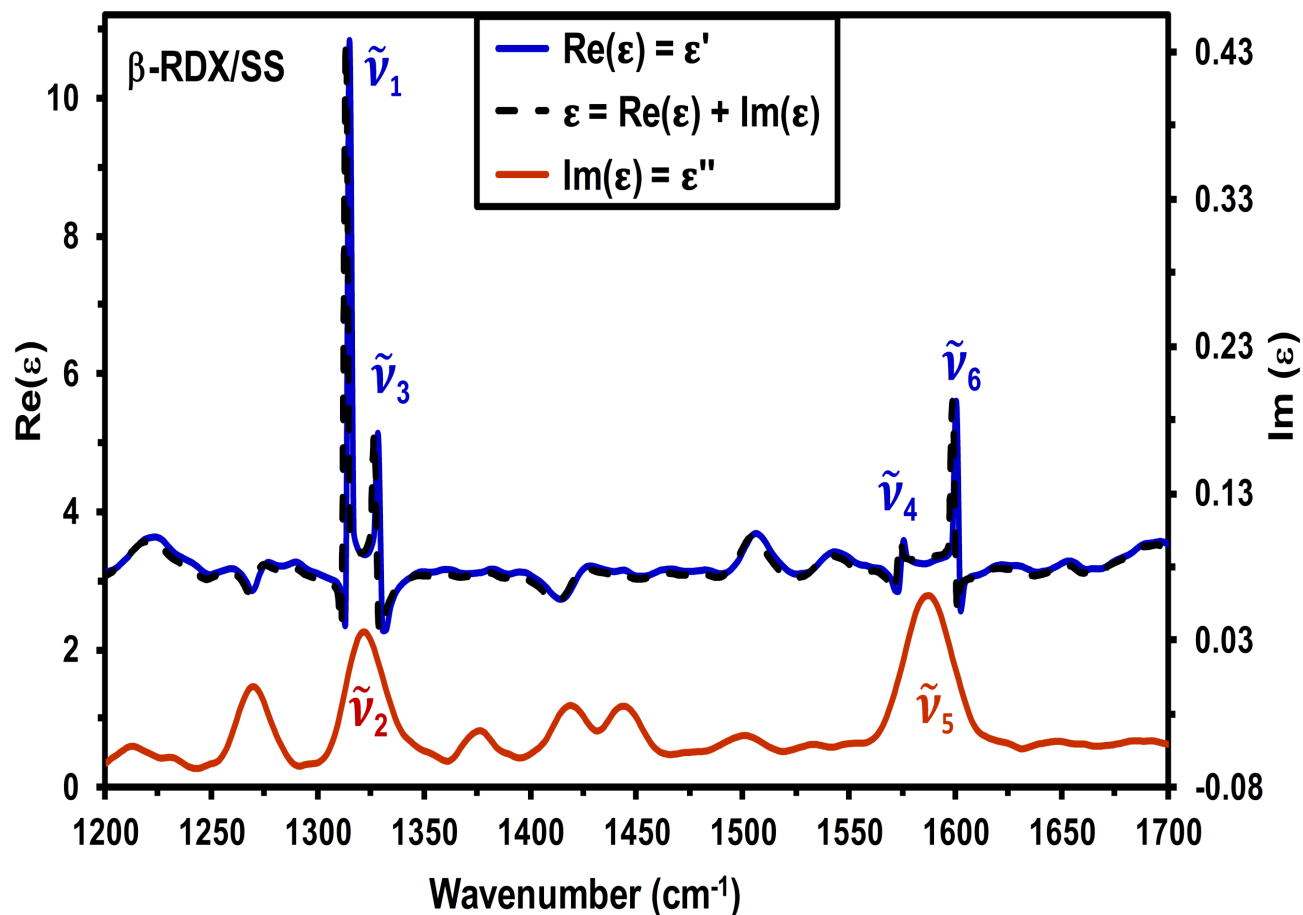


Figure 3–5: Permittivity (ε) of predominantly β -RDX crystalline films deposited on SS substrates (segmented black trace). The transversal optical function is expressed as the imaginary part [$\text{Im}(\hat{\varepsilon})$; red trace] and real part [$\text{Re}(\hat{\varepsilon})$; blue trace] of the permittivity.

In Table 3–2, two maximum values of $\text{Im}[\varepsilon(\tilde{\nu})]$ with respect to the substrate were obtained. These maxima were used to determine the nonzero optical conductivity (γ) for the absorbing media, which is theoretically determined by the following equation:

$$\gamma = \omega \varepsilon_0 \text{Im}(\varepsilon(\tilde{\nu})) \quad (3.2)$$

where ω is the angular frequency. The optical resistivity (ρ) of the absorbing media is the reciprocal of the optical conductivity.

The optical properties of energetic materials have been reported by Isbell and Brewster^{22,25} and Yang et al.³² The results in this contribution are more consistent with the results of Isbell and Brewster.^{22,25} However, Figure 3–6 shows that this contribution was

Table 3–1: Maximum values of the refraction Index [$n(\tilde{\nu})$], extinction coefficient [$k(\tilde{\nu})$], and absorption coefficient [$\alpha(\tilde{\nu})$] for predominantly β -RDX layers deposited on Au and SS.

| Substrate | $\tilde{\nu}(\text{cm}^{-1})$ | $k(\tilde{\nu})$ | $\alpha(\tilde{\nu})$ | $n(\tilde{\nu})$ | Max values (Figure 3–6) |
|-----------|-------------------------------|-----------------------|-----------------------|------------------|----------------------------|
| SS | 1315.26 | 8.92×10^{-4} | 1.475×10^1 | 3.29 | Region I |
| SS | 1321.04 | 8.30×10^{-3} | 1.378×10^2 | 1.84 | |
| SS | 1328.76 | 2.29×10^{-3} | 3.829×10^1 | 2.26 | |
| Au | 1315.26 | 2.34×10^{-2} | 3.874×10^2 | 3.36 | |
| Au | 1322.97 | 1.20×10^{-1} | 1.994×10^3 | 2.14 | |
| Au | 1326.83 | 6.52×10^{-2} | 1.087×10^3 | 2.64 | |
| SS | 1575.61 | 2.85×10^{-3} | 5.649×10^1 | 1.89 | Region II |
| SS | 1587.18 | 1.55×10^{-2} | 3.089×10^2 | 1.80 | |
| SS | 1600.68 | 8.39×10^{-4} | 1.688×10^1 | 2.37 | |
| Au | 1571.75 | 1.85×10^{-1} | 3.678×10^3 | 1.85 | |
| Au | 1587.18 | 1.89×10^{-1} | 3.777×10^3 | 1.85 | |
| Au | 1602.61 | 9.79×10^{-3} | 1.971×10^2 | 2.23 | |

Table 3–2: Maximum values of $\text{Im}(\varepsilon)$ on Au and SS substrates obtained from data shown in Figures 3–4, 3–5. Calculated values of conductivity (γ) and resistivity (ρ) for predominantly β -RDX layers deposited on the two substrates studied were found using Equation 3.2.

| $\tilde{\nu}_2 = 1321.0 \text{ cm}^{-1}$ | | | | $\tilde{\nu}_5 = 1587.2 \text{ cm}^{-1}$ | | | |
|--|--------------------------------|-------------------------------------|-----------------------|--|--------------------------------|-------------------------------------|-----------------------|
| Substrate | $\text{Im}(\hat{\varepsilon})$ | γ (ohm · m) ⁻¹ | ρ (ohm · m) | Substrate | $\text{Im}(\hat{\varepsilon})$ | γ (ohm · m) ⁻¹ | ρ (ohm · m) |
| Au | 0.51 | 1.13×10^3 | 8.85×10^{-4} | Au | 0.70 | 1.85×10^3 | 5.39×10^{-4} |
| SS | 0.03 | 6.75×10^1 | 1.48×10^{-2} | SS | 0.06 | 1.48×10^2 | 6.76×10^{-3} |

also consistent with the results of Yang et al.³²: they have the same order of magnitude, although the experimental setups were markedly different. Table 3–3 summarizes the experimental details of the three methodologies used to obtain the optical properties of RDX in the MIR region. Three different thicknesses were studied, but only the present contribution focused on thin RDX films. Finally, three angles of incidence were used to obtain the relevant information to calculate the desired optical properties. The important factor is that the optical properties determined by various methodologies were consistent in terms of the order of magnitude of the obtained values. However, this contribution includes two

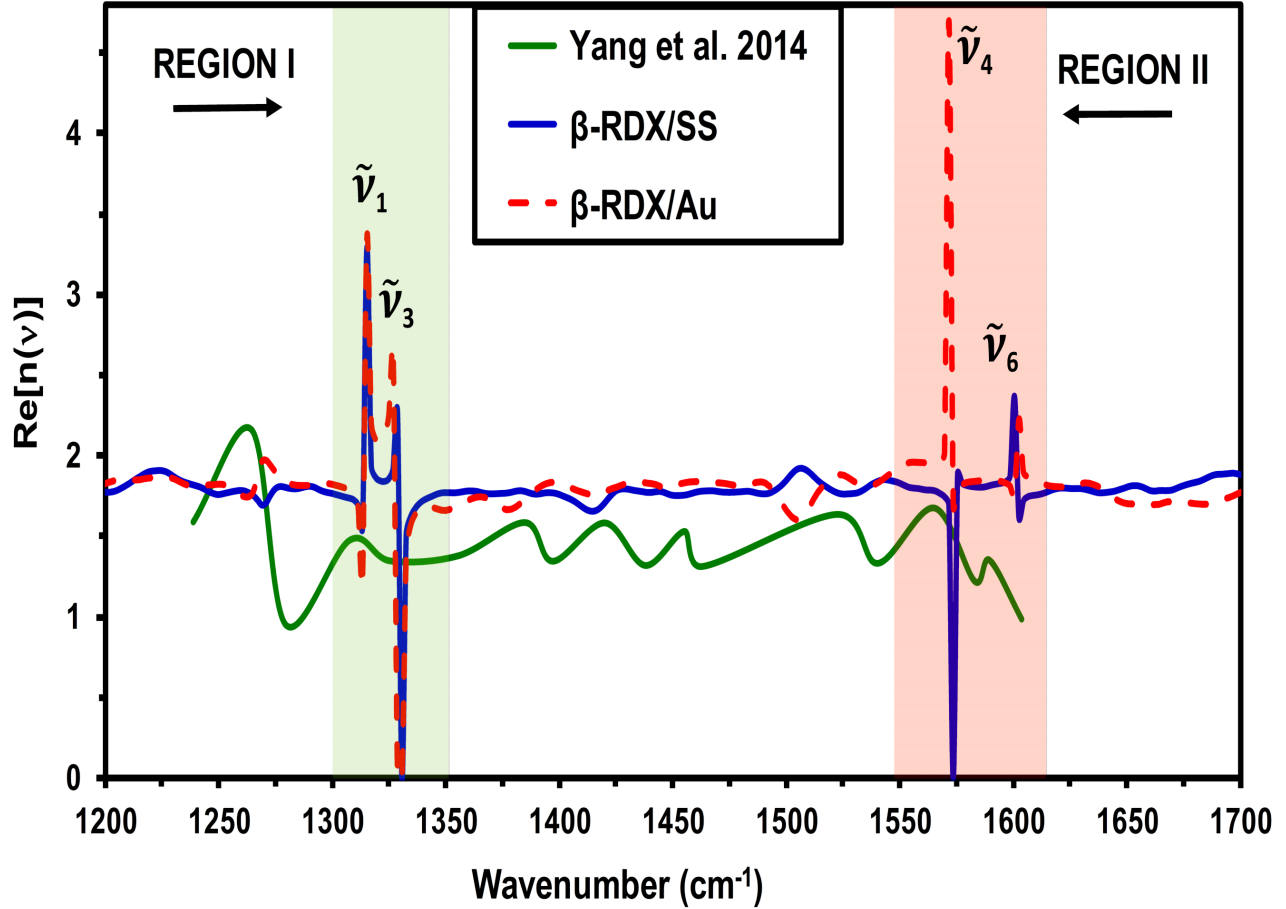


Figure 3–6: Comparison of the refractive index of RDX thin films from this contribution with literature values. RDX/ZnSe-ATR (Yang et al.²⁹; green trace); β -RDX/SS (blue trace); β -RDX/Au (segmented red trace).

important characteristics: (i) the longitudinal and transverse optical vibrations are not mediated by the substrate; (ii) the real part of the refractive index, $\text{Re}[n(\tilde{\nu})]$, behaves similarly to the real part of the permittivity, $\text{Re}[\varepsilon(\tilde{\nu})]$.

Many differences appear in the ranges of $1250\text{--}1350\text{ cm}^{-1}$ and $1550\text{--}1625\text{ cm}^{-1}$ in Figure 3–6. In the range of the symmetric stretching of the nitro groups ($1250\text{--}1350\text{ cm}^{-1}$), both SS and ZnSe substrates shift the peak maximum. This result is in contrast to the behavior of the Au substrate, where the maximum peak appears in the region of the nitro group asymmetric stretching (1575.6 cm^{-1}), and no shifting is observed. As previously discussed, the maximum peaks of $\text{Re}[n(\tilde{\nu})]$ and $\text{Re}[\varepsilon(\tilde{\nu})]$ are activated by both (a) the incident angle of infrared light traversing the RDX layer and (b) the type of substrate. Some efforts have

Table 3–3: Comparison of various experimental setups and conditions used to obtain the optical properties of RDX in the MIR region.

| Authors (yr) | Incident angle | Methodolog substrates | Technique | Thichness (h) | Source Polaization |
|-------------------------------|-------------------|--------------------------|--------------|------------------------------|-----------------------|
| Isbell- Brewster (1998) | 0° | FTIR/ KBr pellet | Trasmission | 0.5 μm < h < 1 cm | none |
| Yang et al. (204) | 45° | ZnSe ATR* | Ellipsometry | < 20 μm | s & p |
| This work | 80° | Au, SS | RAIRS | 2 nm < h < 200 nm | s & p |

*zinc selenide attenuated total reflectance

been directed to study the splitting of $\tilde{\nu}_{\text{TO}}$ and $\tilde{\nu}_{\text{LO}}$ which is also an interesting topic of discussion.⁴⁷ The authors concur that the splitting of bands arises from perturbations of the electric field owing to the induced dipole moments.⁴⁷ In fact, Yamamoto and coworkers⁴⁰ have mentioned in their conclusions that the shifts in peak position and changes in peak shapes may be because of the TO-LO splitting in the spectra at oblique angles of incidence.⁴⁶ The same observation was made by Tolstoy and coworkers.³³

3.4 CONCLUSIONS

RAIRS measurements were used to obtain the optical constants of β -RDX thin crystalline films deposited on Au and SS substrates. The theoretical equations required to calculate the optical properties of the thin films were effectively used to analyze the MIR measurement results. The refractive index $n(\tilde{\nu})$, absorption coefficient $\alpha(\tilde{\nu})$, and absorption index $k(\tilde{\nu})$ of β -RDX films, which were calculated from the MIR-RAIRS measurements, were consistent with the reported values in the literature, although the reported spectral range was much wider and the angle of incidence of the MIR radiation was much steeper. Considering that recent reports did not measure the optical properties using RAIRS, these results intend to update previous reports of a polymorphic energetic material. Regarding the contributions of the substrates to the optical properties of the adsorbate, these results can be attributed to the reflectivity of the substrate. Au substrates are more reflective than SS substrates, as proven by the data and calculated values. In addition, β -RDX (adsorbate)

shows a response that intensifies both transversal ($\tilde{\nu}_{\text{TO}}$) and longitudinal ($\tilde{\nu}_{\text{LO}}$) optical vibrations. This sensitivity manifestation is depicted by $\tilde{\nu}_{\text{TO}} = \tilde{\nu}_{\text{LO}}$ for both substrates at 1587.2 cm^{-1} . $\tilde{\nu}_{\text{TO}}$ (or $\tilde{\nu}_{\text{LO}}$) becomes sensitive for β -RDX/Au (or β -RDX/SS) crystalline films through the asymmetric stretch of the axial $-\text{NO}_2$ groups. Furthermore, $\text{Re}[n(\tilde{\nu})]$ and $\text{Re}[\varepsilon(\tilde{\nu})]$ show similar behaviors when β -RDX is deposited on SS and Au, which splits the two maximum peaks in the $1250\text{--}1350 \text{ cm}^{-1}$ and $1550\text{--}1625 \text{ cm}^{-1}$ ranges, respectively.

REFERENCE LIST

- [1] A.M. Figueroa-Navedo, J.L. Ruiz-Caballero, L.C. Pacheco-Londoño, and S.P. Hernández-Rivera. Characterization of α - and β -rdx polymorphs in crystalline deposits on stainless steel substrates. *J. Cryst. Growth Des.*, 16(7):3631–3638, 2016.
- [2] E.D. Emmons, M.E. Farrell, E.L. Holthoff, A. Tripathi, N. Green, R.P. Moon, J.A. Guicheteau, S.D. Christesen, P.M. Pellegrino, and A.W. Iii, Fountain. Characterization of polymorphic states in energetic samples of 1,3,5-trinitro-1,3,5-triazine (rdx) fabricated using drop-on-demand inkjet technology. *Appl. Spectrosc.*, 66:628–635, 2012.
- [3] B.J. Baer, J. Oxley, and M. Nicol. The phase diagram of rdx (hexahydro -1,3,5-trinitro-triazine) under hydrostatic pressure. *High Pressure Res.*, 2:99–108, 1990.
- [4] P.J. Miller, S. Block, and G. Piermarini. Effects of pressure on the thermal decomposition kinetics, chemical reactivity and phase behavior of rdx. *J. Combust. Flame.*, 83:174–184, 1991.
- [5] P. Torres, L. Mercado, I. Cotte, S.P. Hernández, N. Mina, A. Santana, R.T. Chamberlain, R. Lareau, and M.E. Castro. Vibrational spectroscopy study of beta and alpha rdx deposits. *J. Phys. Chem. B.*, 108:8799–8805, 2004.
- [6] Z.A. Dreger and Y.M. Gupta. Raman spectroscopy of high-pressure-high-temperature polymorph of hexahydro-1,3,5-trinitro-1,3,5-triazine (ϵ -rdx). *J. Phys. Chem. A.*, 114(26):7038–7047, 2010.
- [7] J.W. Kim, J.K. Kim, H.S. Kim, and K.K. Koo. Characterization of liquid inclusion of rdx crystals with a cooling crystallization. *Cryst. Growth Des.*, 9(6):2700–2706, 2009.
- [8] I.G. Goldberg and J.A. Swift. New insights into the metastable β form of rdx. *J. Cryst. Growth Des.*, 12:1040–1045, 2012.
- [9] *Explosives engineering*, volume Eighth. Wiley-VCH, 1996. ISBN: 978-0-471-18636-6.

- [10] W. McCrone. Crystallographic data. 32. rdx (cyclotrimethylenetrinitramine). *Anal. Chem.*, 22(7):954–955, 1950.
- [11] C.S. Choi and E. Prince. The crystal structure of cyclotrimethylenetrinitramine. *Acta Cryst. B.*, 28(9):2857–2852, 1972.
- [12] R. Infante-Castillo, L.C. Pacheco-Londoño, and S.P. Hernández-Rivera. Vibrational spectra and structure of rdx and its 13c- and 15n-labeled derivatives: A theoretical and experimental study. *Spectrochim. Acta, Part A.*, 76(2):137–141, 2010.
- [13] R. Infante-Castillo, L.C. Pacheco-Londoño, and S.P. Hernández-Rivera. Monitoring the $\alpha \rightarrow \beta$ solidsolid phase transition of rdx with raman spectroscopy: A theoretical and experimental study. *J. Mol. Struct.*, 970(1):51–58, .
- [14] R.J. Karpowicz, S.T. Sergio, and T.B. Brill. β -polymorph of hexahydro-1, 3, 5-trinitro-s-triazine. a fourier transform infrared spectroscopy study of an energetic material. *Ind. Eng. Chem. Prod. Res. Dev.*, 22(2):363–365, 1983.
- [15] R.J. Karpowicz and T.B. Brill. Comparison of the molecular structure of hexahydro-1, 3, 5-trinitro-s-triazine in the vapor, solution, and solid phases. *J. Phys. Chem.*, 88(3):348–352, 1984.
- [16] H.G. Gallagher, R.M. Vrcelj, and J.N. Sherwood. The crystal growth and perfection of 2,4,6-trinitrotoluene. *J. Cryst. Growth. Des.*, 250(3):486–498, .
- [17] G. Gillen, C. Zeissler, C. Mahoney, A. Lindstrom, P. Fletcher, R.; Chi, J. Verkouteren, D. Bright, R.T. Lareau, and M. Boldman. Automated analysis of organic particles using cluster sims. *Appl. Surf. Sci.*, 231:186–190, 2004.
- [18] M. Wrable-Rose, O.M. Primera-Pedrozo, L.C. Pacheco-Londoño, and S.P. Hernández-Rivera. Preparation of tnt, rdx and ammonium nitrate standards on gold-on-silicon surfaces by thermal inkjet technology. *Sens. Imaging.*, 11(4):147–169, 2010.
- [19] E. Windsor, M. Najarro, A. Bloom, B. Banner Jr, R. Fletcher, R. Lareau, and G. Gillen. Application of inkjet printing technology to produce test materials of 1,3,5-trinitro-1,3,5 triazacyclohexane for trace explosive analysis. *Anal. Chem.*, 82(20):8519–8524, 2010.

- [20] A.C. Ihnen, A.M. Petrock, T. Chou, P.J. Samuels, B.E. Fuchs, and W.Y. Lee. Crystal morphology variation in inkjet-printed organic materials. *Appl. Surf. Sci.*, 258(2):827–833, 2011.
- [21] J.R. Verkouteren, J. Lawrence, G.A. Klouda, M. Najarro, J. Grandner, R.M. Verkouteren, and S.J. York. Performance metrics based on signal intensity for ion mobility spectrometry based explosive trace detectors using inkjet printed materials. *Analyst.*, 139(21):5488–5498, 2014.
- [22] R.A. Isbell and M.Q. Brewster. Optical properties of rdx and hmx. *Mater. Res. Soc. Symp. Proc.*, 418:85, 2011.
- [23] D.L. Allara, A. Baca, and C.A. Pryde. Distortions of band shapes in external reflection infrared spectra of thin polymer films on metal substrates. *Macromolecules.*, 11(6):1215–1220, 1978.
- [24] O.S. Heavens. Thin film research today. *Nature.*, 228(5276):1036–1039, 1970.
- [25] R.A. Isbell and M.Q. Brewster. Optical properties of energetic materials, rdx, hmx, ap, nc/ng, and htpb. *Propellants, Explos., Pyrotech.*, 23(4):218–224, 1998.
- [26] O. Primera-Pedrozo, Y. Soto-Feliciano, L. Pacheco-Londoño, and S. Hernández-Rivera. Detection of high explosives using reflection absorption infrared spectroscopy with fiber coupled grazing angle probe/ftir. *Sensing and imaging. An International Journal.*, 10(1):1–13, 2009.
- [27] R.G. Greenler. Infrared study of absorbed molecules on metal surfaces by reflection techniques. *J. Chem. Phys.*, 44:310–314, 1996.
- [28] P.B. Johnson and R.W. Christy. Optical constants of the noble metals. *Phys. Rev. B.*, 6(12):4370, 1972.
- [29] L.C. Pacheco-Londoño, W. Ortiz-Rivera, O.M. Primera-Pedrozo, and S.P. Hernandez-Rivera. Vibrational spectroscopy standoff detection of explosives. *Anal. Bioanal. Chem.*, 395(2):323–335, 2009.

- [30] N.J. Galan-Freyte, L.C Pacheco-Londoño, A.M. Figueroa-Navedo, and S.P. Hernandez-Rivera. Standoff detection of highly energetic materials using laser-induced thermal excitation of infrared emission. *Appl. Spectrosc.*, 69(5):535–544, 2015.
- [31] R.G. Greenler, R.R. Rahn, and J.P. Schwartz. The effect of index of refraction on the position, shape, and intensity of infrared bands in reflection-absorption spectra. *J. Catal.*, 23(1):42–48, 1971.
- [32] C.S. Yang, B.R. Williams, A. Tripathi, M.S. Hulet, A.C. Samuels, J.A. Domanico, J. May, R.W. Miles Jr, and A.W. Fountain III. Spectral characterization of rdx, etn, petn, tatp, hmted, hmx, and c-4 in the mid-infrared region. (no. ecbc-tr-1243). Technical report, DTIC Document, Maryland, 2014. U.S. Army Edgewood Chemical Biological Center: Aberdeen Proving Ground.
- [33] V.P. Tolstoy, V.A. Chernyshova, and V.P. Skryshevsky. *Handbook of infrared spectroscopy of ultrathin films*. John Wiley & Sons, Inc., Hoboken, NJ., 2003. ISBN: 9780471234326.
- [34] A. Sengupta, S. Herminghaus, and C. Bahr. Liquid crystal microfluidics: surface, elastic and viscous interactions at microscales. *Liq. Cryst. Rev.*, 2(2):73–110, 2014.
- [35] A.O. Kivioja, Anna-Stiina J a askel ainen, V. Ahtee, and T. Vuorinen. Thickness measurement of thin polymer films by total internal reflection raman and attenuated total reflection infrared spectroscopy. *Vib. Spectrosc.*, 61:1–9, 2012.
- [36] W. Bachmann and J.C. Sheehan. A new method of preparing the high explosive rdx. *J. Am. Chem. Soc.*, 71:1842–1845, 1949.
- [37] P. Hollins and J. Pritchard. Infrared studies of chemisorbed layers on single crystals. *Prog. Surf. Sci.*, 19(4):275–349, 1985.
- [38] R.G. Greenler. Design of a reflection-absorption experiment for studying the ir spectrum of molecules adsorbed on a metal surface. *J. Vac. Sci. Technol.*, 12:1410, 1975.
- [39] C.H. Liu and X. Yu. Silver nanowire-based transparent, flexible, and conductive thin film. *Nanoscale Res. Lett.*, 6:75, 2011.

- [40] Y.C. Lu and K.S. Chou. Tailoring of silver wires and their performance as transparent conductive coatings. *Nanotechnology.*, 21(21):215707–215713, 2010.
- [41] M.A. Barreto-Cabn, L.C. Pacheco-Londoño, M.L. Ramírez, and S.P. Hernández-Rivera. Novel method for the preparation of explosive nanoparticles. *Proc. SPIE.*, 6201(9):620129–62013, 2006.
- [42] M. Chwastek, J. Weszka, J. Jurusik, B. Hajduk, and P. Jarka. Influence of technological conditions on optical properties and morphology of spin-coated ppi thin films. *Arch. Mater. Sci. Eng.*, 48(2):69–76, 2011.
- [43] J.C. Maxwell. *A Treatise on Electricity and Magnetism Unabridged.*, volume one. Dover Publication, Inc., New York, NY., 3th edition, 1954. ISBN: 486-60636-8.
- [44] K. Yamamoto and H. Ishida. Optical theory applied to infrared spectroscopy. *Vib. spectrosc.*, 8(1):1–36, 1994.
- [45] C. Kittel. *Introduction to Solid State Physics*. John Wiley & Sons, Inc., Danves, MA., eighth edition, 2005. ISBN : 978-0-471-41526-8.
- [46] N.W. Ashcroft and N.D. Mermin. *Solid state physics*. Holt, Rinehart and Winston, New York, NY, 1976. ISBN: 0-03-083993-9.
- [47] K. Yamamoto and H. Ishida. Interpretation of reflection and transmission spectra for thin films: Reflection. *Appl. Spectrosc.*, 48(7):775–787, 1994.
- [48] L.C. Pacheco-Londoño, A. Santiago, J. Pujols, O.M. Primera-Pedrozo, A. Mattei, W. Ortiz, O. Ruiz, M. Ramírez, and S.P. Hernandez-Rivera. Characterization of layers of tetryl, tnb and hmx on metal surfaces using fiber optics coupled grazing angle-ftir. *Proc. SPIE*, 6542:1–3, 2007. doi: 10.1117/12.720976.

CHAPTER 4

CONCLUSIONS

4.1 GENERAL IMPLICATIONS

The presented results show the best conditions to obtain predominantly β RDX crystalline films deposited in both substrates stainless steel and gold. All the characterization carried out emphasizes in the interests to the development of samples and standards using spin coating technology at laboratory conditions. It is important to emphasize that in solid state α -RDX is the most stable conformation and that preparing a predominantly β -RDX conformation ensemble is not a simple task. However, α/β -RDX polymorphs exhibit morphological variations within substrates. These crystalline formations include: dendrites, island, and prisms. Table 2.1 shows rotational speed parameters to obtain binary samples regarding to experiments that require a fine distribution control of analytes on surfaces. Differentiation of the polymorphs was based on FT-IR vibrational signatures and assignments correlated with the reported values in literature for the α - and β -RDX. RDX polymorphs coexistence was also confirmed by Raman spectra. RAIRS spectra were averaged for the CH region. With this spectroscopic information, polymorphic features were visualized using PCA. In fact, these spectral features should provide information for generating spectral libraries for defense, security, and forensic applications. The characterization of these structures by AFM and white light microscopy provided evidence of a extreme change in morphology as angular speed increased. The most important aspect in this study remains the solvent's mediation of converting the β RDX polymorph to α RDX. Further evidence of

Stranski-Krastanov formation were demonstrated by the presence of solvent in the contiguous areas to α -RDX crystals. This supports the hypothesis of solvent-mediated conversion from β -RDX to α -RDX.

The optical properties were determined for the β RDX polymorph which predominates on gold and stainless steel substrates at 3k rpm. This predominance makes the crystals, in the form of dendrites, favor films with most homogeneity. However, at lower rotational speeds, the samples lost homogeneity. Due to the mathematical model used, it was required that the crystalline film has a thickness in the order of $> 0.2 \mu\text{m}$. The results the calculations of the optical properties and in particular, the real part of refractive index $\text{Re}(n(\tilde{\nu}))$ were consistent with the reported values in the literature. Considering that recent reports did not measure the optical properties using RAIRS, these results intend to update previous reports of a polymorphic energetic material. Furthermore, $\text{Re}[n(\tilde{\nu})]$ and $\text{Re}[\varepsilon(\tilde{\nu})]$ show similar behaviors when β -RDX is deposited on SS and Au, which splits the two maximum peaks in the $1250\text{--}1350 \text{ cm}^{-1}$ and $1550\text{--}1625 \text{ cm}^{-1}$ ranges, respectively. These peaks maxima also indicate significant energy absorption as a dynamic response of vibrational modes. As future applications these crystalline β -RDX film samples could be used as possible light filters.

4.2 FUTURE WORKS

In order to give continuity to the development of samples, more HEM could be worked in addition to the RDX, i.e. pentaerythritol tetranitrate (PETN), 2,4,6-trinitrotoluene (TNT), 2,4-dinitrotoluene or 2,6-dinitrotoluene (DNT), ammonium nitrate (AN), octahydro-1,3,5,7-tetranitro-1,3,5,7-tetrazocine (HMX), triacetone triperoxide (TATP), diacetone diperoxide (DADP), and mixtures. On the other hand, the research could breach in other metallic substrates such as copper, platinum and aluminum. In fact, it is also important to evaluate different deposition methodologies such as inkjet, smearing and drop cast.

As an enrichment of the exposed investigation, the X-ray diffraction technique could be used as an alternative technique to corroborate the crystalline polymorphism shown in Table

2.1. Also, AFM coupled to Raman could be integrated to acquire a detailed topographic analysis with the assignment of characteristic Raman active modes.

APPENDICES

APPENDIX A

SUPPLEMENTAL MATERIAL FROM CHAPTER TWO

Additional information includes FT-IR-RAIS spectra of thin RDX films deposited on SS substrates acquired at various incident angles and used to obtain the optimum incidence angle for the study. It also includes Raman spectra of fibers for 8k rpm deposits and Raman spectra of dendrites for 3k rpm deposits.

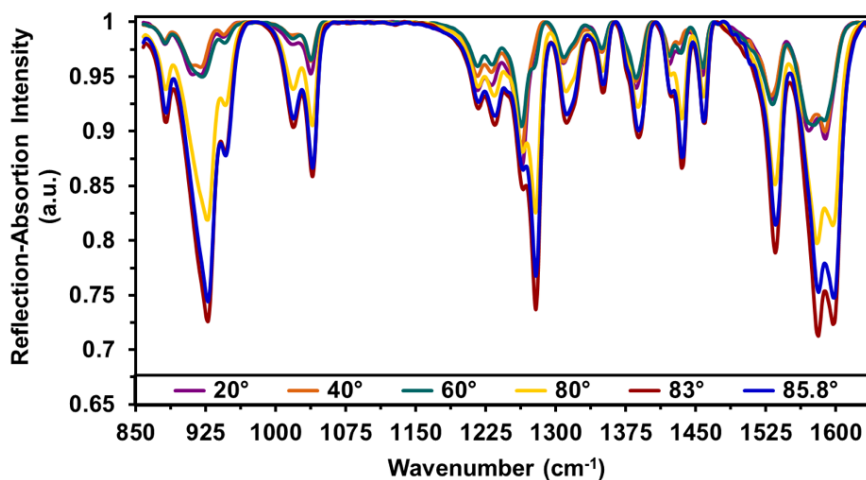


Figure A-1: RAIRS spectra thin RDX films deposited on SS substrates at various incidence angles.

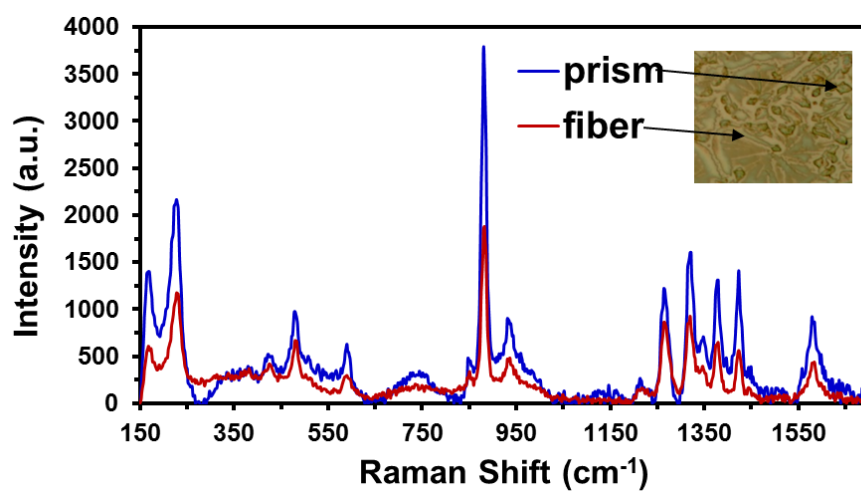


Figure A-2: Raman spectra for 8k rpm showing higher intensity for the prism structure than the fibers examined.

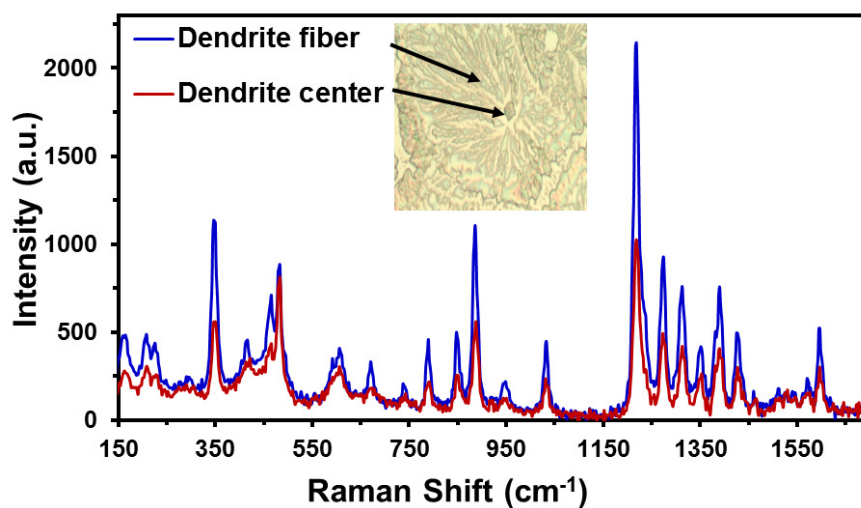


Figure A-3: Raman spectra for 3k rpm showing intensity variations depending on the structural topology of the surface.

APPENDIX B

SUPPLEMENTAL MATERIAL FROM CHAPTER THREE

This section includes five figures: (B-1) RAIRS spectra excited with polarized light of predominantly β -RDX crystalline films on an Au substrate compared to spectrum with unpolarized light; (B-2) RAIRS spectra excited with polarized light of predominantly β -RDX crystalline films on SS substrate compared with spectrum acquired with unpolarized light; (B-3) Imaginary part of the permittivity (ε) of predominantly β -RDX crystalline films deposited on (a) gold substrates, and (b) SS substrates; (B-4) Extinction coefficient $k(\tilde{\nu}) = \text{Im}[n(\tilde{\nu})]$ of predominantly β -RDX crystalline films deposited on Au and SS substrates; (B-5) Absorption coefficient $[\alpha(\tilde{\nu})]$ of predominantly β -RDX crystalline films deposited on Au and SS substrates.

In Figure B-1, solvent modes are indicated with solid black guide arrows, and the dashed red arrows represent vibrational modes corresponding to the solvent and/or of the α -RDX polymorph.

Solvent bands are indicated with black solid arrow guidelines. The red dashed arrow guidelines represent vibrational modes corresponding to the solvent and very small amounts of the α -RDX polymorph. The same scales as in Figure B-1 have been maintained for purposes of comparison of the intensities of the bands observed on the two substrates.

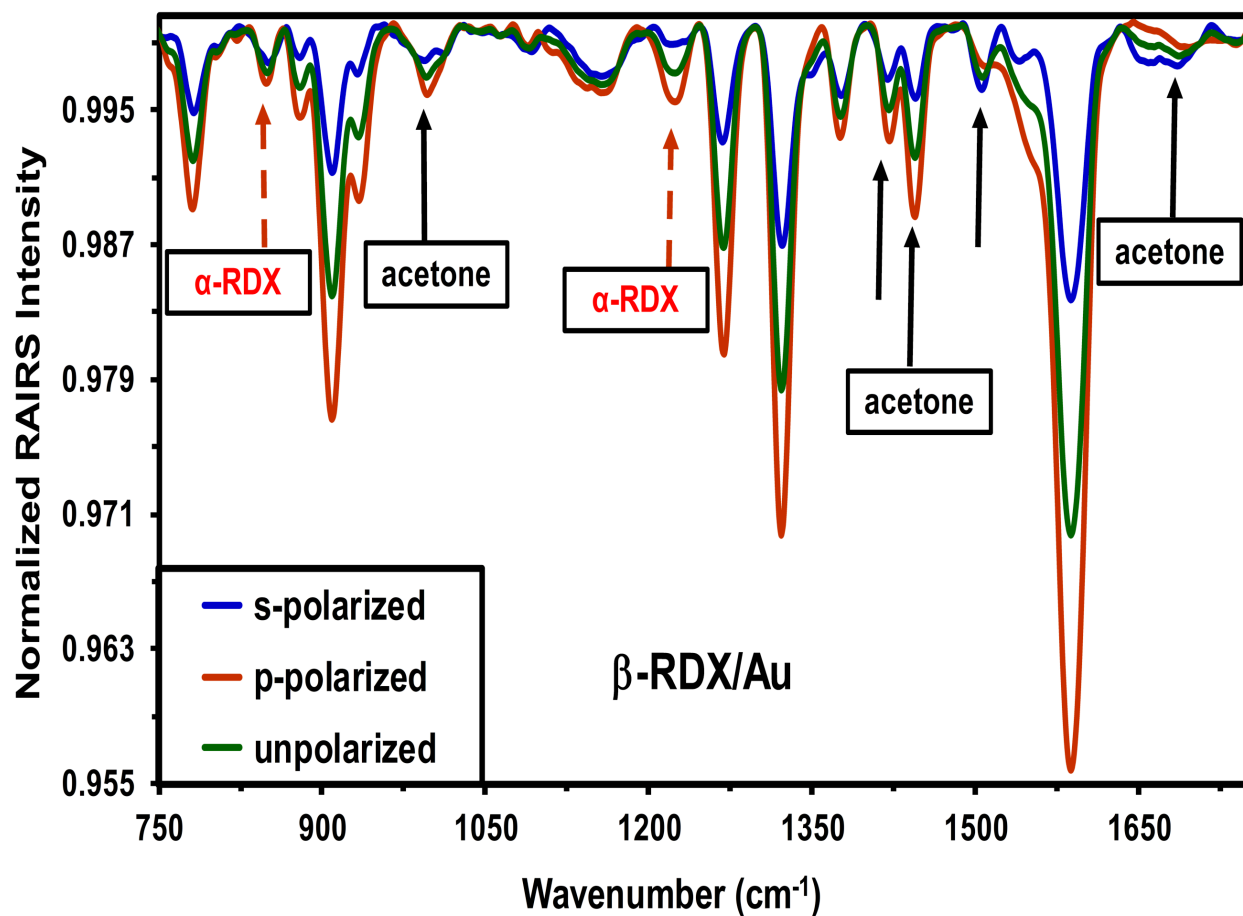


Figure B-1: RAIRS spectra with excited with polarized light (s & p polarizations) of predominantly β -RDX crystalline films on Au substrate compared with spectra obtained with unpolarized light. Spectrum with s-polarized light is illustrated by the blue trace; spectrum acquired with p-polarized light is represented by the red trace, and spectrum with unpolarized light is shown as the green trace.

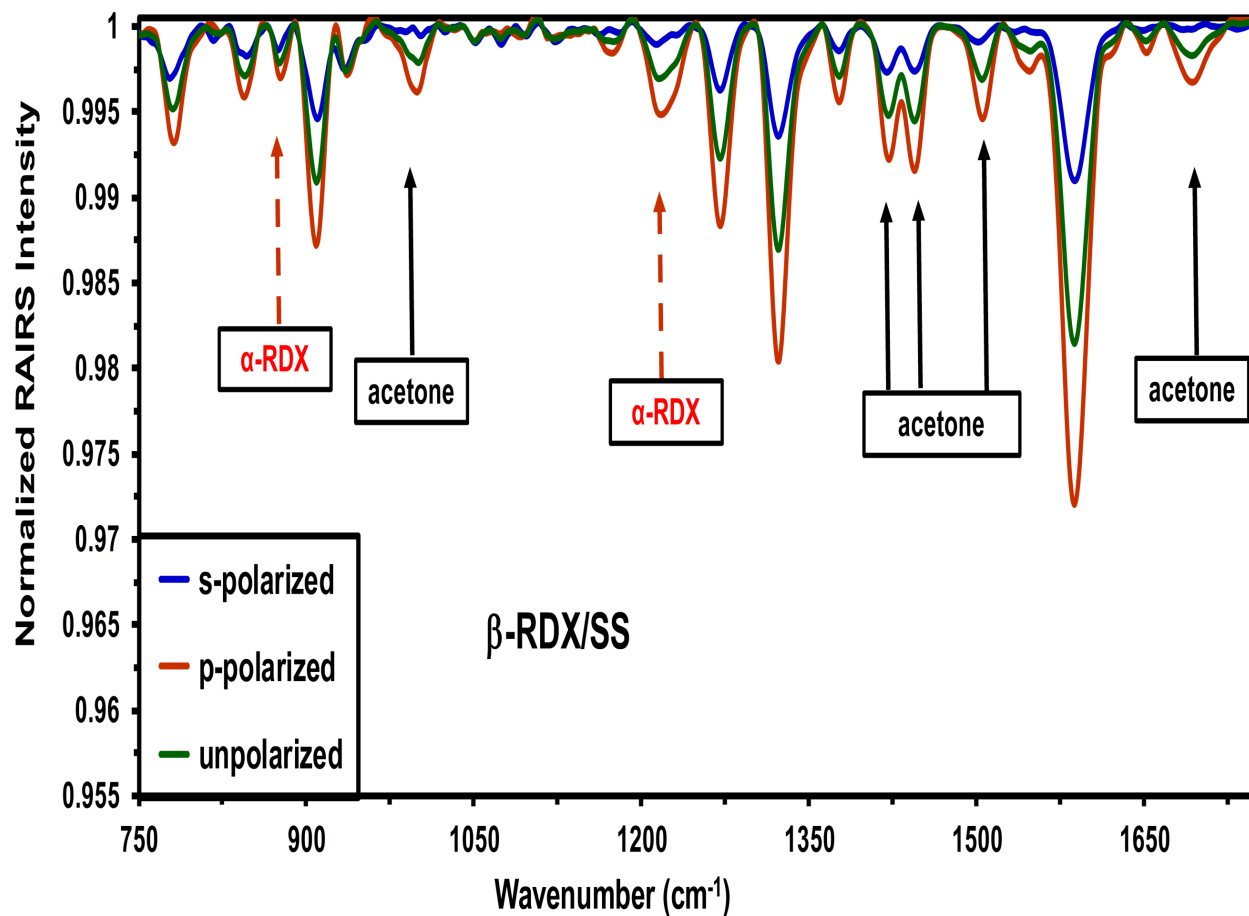


Figure B–2: RAIRS spectra excited with polarized light (s & p polarizations) of predominantly β -RDX crystalline films on SS substrate compared with spectrum obtained with unpolarized light. Spectrum acquired with s-polarized light is illustrated by blue trace; spectrum excited with p-polarized light is represented by the red trace; spectrum obtained with unpolarized light is shown as green trace.

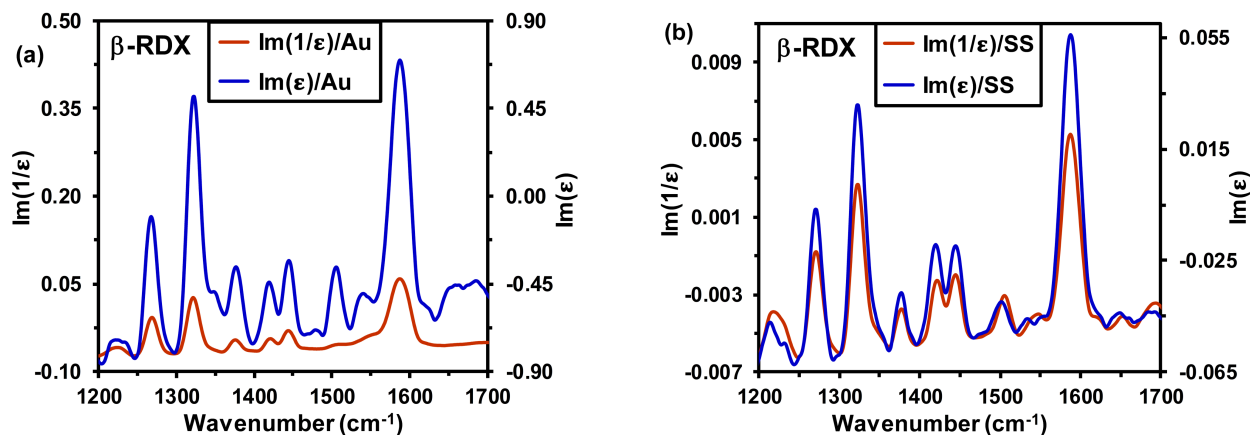


Figure B–3: Imaginary part of the permittivity (ε) of predominantly β -RDX crystalline films deposited on (a) gold substrates, and (b) stainless steel substrates. The blue trace corresponds to the imaginary part of the inverse of permittivity ($1/\varepsilon$), and the red trace corresponds to the imaginary part of the permittivity ($\text{Im}(\varepsilon)$; secondary “y” axis).

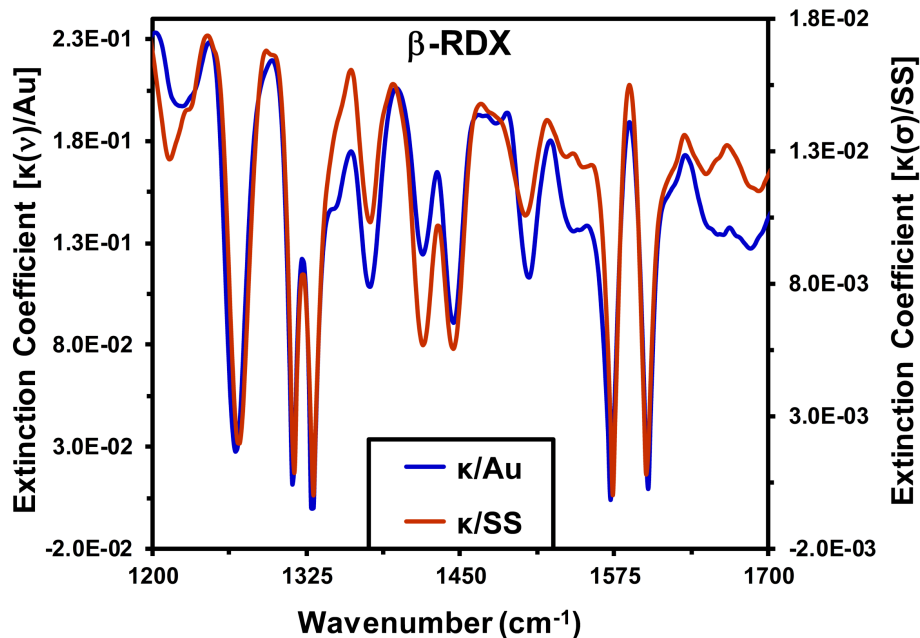


Figure B–4: Extinction coefficient [$k(\tilde{\nu}) = \text{Im}(n(\tilde{\nu}))$] of predominantly β -RDX crystalline films deposited on Au (blue trace; principal “y” axis), and SS (red trace; secondary “y” axis).

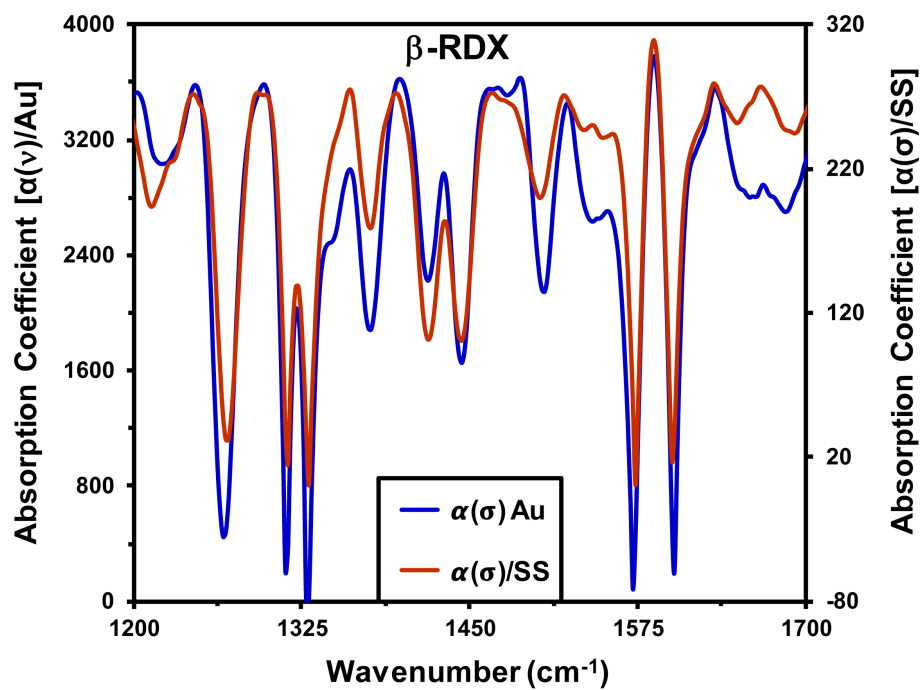


Figure B-5: Absorption coefficient [$\alpha(\tilde{\nu})$] of predominantly β -RDX crystalline films deposited on Au (blue trace; principal “y” axis), and SS (red trace; secondary “y” axis).